

A preliminary evaluation of FY-4A visible radiance data assimilation by the WRF (ARW v4.1.1)/DART (Manhattan release v9.8.0)-RTTOV (v12.3) system for a tropical storm case

Yongbo Zhou^{1,2}, Yubao Liu^{1,2}, Zhaoyang Huo^{1,2}, Yang Li^{1,2}

5 ¹School of Atmospheric Physics, Nanjing University of Information Science and Technology, Nanjing, China

²Precision Regional Earth Modeling and Information Center (PREMIC), Nanjing University of Information Science and Technology, Nanjing, China

Correspondence to: Yongbo Zhou (yongbo.zhou@nuist.edu.cn)

Abstract. Satellite visible radiance data **that** contain rich cloud and precipitation information are increasingly assimilated for improving **forecasts** of numerical weather prediction models. This study evaluates the Data Assimilation Research Testbed (DART, Manhattan release v9.8.0), coupled with the Weather Research and Forecasting (WRF) model (ARW v4.1.1) and the Radiative Transfer for TOVS (RTTOV, v12.3) package, for assimilating the simulated visible imagery of the FY-4A geostationary satellite located over Asia **in an** Observing System Simulation Experiment (OSSE) **framework**. The OSSE was performed for a Tropical Storm named Higos **occurred in 2020** that contains multi-layer mixed-phase cloud and precipitation processes. **The advantages and limitations of DART for assimilating FY-4A visible imagery were evaluated.** Both single observation experiments and cycled **DA** experiments were performed to study the **impact** of different filter algorithms **available in DART, variables being cycled, observation outlier thresholds, observation errors, and observation thinning.**

The results show that assimilating visible radiance data significantly improves the analysis of cloud water path (CWP) and cloud coverage (CFC) **from the first-guess forecasts.** The Rank Histogram Filter (RHF) allows WRF to more accurately simulate CWP and CFC than the Ensemble Adjustment Kalman Filter (EAKF) although it took roughly twice time of the later. By cycling both cloud and non-cloud variables, specifying large outlier threshold values, or setting smaller observation errors **without thinning of observations, WRF achieved better simulation of CWP and CFC.** With model integration, **DA** of the visible radiance data also generated slightly positive **impact** on non-cloud variables as they were adjusted through the model dynamics and physics related to cloud processes. In addition, the **DA** improved the representation of precipitation. However, the **impact** on rain rate is limited by the inabilities of the **DA** to improve cloud vertical structures and cloud phases. Some negative **impact** of the **DA** on cloud variables was found due to the nature of the non-linear forward operator and the non-Gaussian distribution of the prior. Future works should explore faster and more accurate forward operators suitable for assimilating FY-4A visible imagery, techniques to reduce the non-linear and non-Gaussian errors, methods to correct the location errors **which correspond to the underestimated clouds by the first guess**, etc.

1. Introduction

All-sky satellite data assimilation (DA) has shown great potential to improve weather forecasts (Bauer et al., 2011). Many satellite DA-related studies were done for microwave (MW) and infrared (IR) radiance data. DA of MW radiance data adjusts the atmospheric state variables such as humidity and temperature (Geer et al., 2019; Migliorini and Candy, 2019) as well as cloud-related parameters such as cloud water/ice content and cloud coverage (Zhang et al., 2013; Yang et al., 2016), exhibiting positive effects on cloud and precipitation forecasting. All-sky MW data has been operationally assimilated at some Numerical Weather Prediction (NWP) centres (Bauer et al., 2010; Zhu et al., 2016). However, operational DA of all-sky MW data is limited to humidity- and temperature-sounding channels (Carminati and Migliorini, 2021) because MW radiance at these channels is insensitive to surface emissivity and skin temperature which are difficult to be estimated accurately under cloudy sky conditions (Hu et al., 2021a). DA of MW data is also challenging in terms of separating the radiance contribution of clouds from the non-cloud variables (especially temperature and humidity) (Geer et al., 2017). In addition, several existing studies showed positive effects on water vapour and temperature by assimilating the IR data in clear sky (McCarty et al., 2009; Ma et al., 2017). DA of IR radiance data in cloudy regions also improved the analysis of column integrated water and forecasting skills in the mid- and upper troposphere (Stengel et al., 2013; Geer et al., 2019). However, DA of IR radiance data in cloudy regions is still complicated by the non-linear relationship between the observation and state variables, the non-Gaussian problems (Li et al., 2022), the difficulty to separate cloud signals and non-cloud signals (Geer et al., 2017), and the inability to constrain the layered structures in the case of multi-layer clouds (Prates et al., 2014).

Several earlier studies suggested that there is great potential to assimilate the visible (VIS) and shortwave infrared (collectively referred to as shortwave, SW) data (Vukicevic et al., 2004; Polkinghorne and Vukicevic, 2011; Scheck et al., 2020; Schrötle et al., 2020) because these measurements contain some unique and supplementary cloud information to the IR and MW radiance data (Kostka et al., 2014; Schrötle et al., 2020). For example, SW radiation can penetrate a certain depth of cloud fields, and connotate cloud microphysical properties such as effective particle radius (Nakajima and King, 1990). In comparison, satellite IR data only provide information on the cloud top microphysics (Xue, 2009). SW data also complement precipitation radars that mainly measure large hydrometeors or precipitation particles (Keat et al., 2019) that usually do not occur during the initial growth stage of convective systems (Zhang and Fu, 2018), measuring mainly small cloud droplets. Furthermore, SW data usually have higher spatial resolution than MW data (Yang et al., 2017; Coste et al., 2017; Schmit et al., 2018). Therefore, high-resolution satellite SW radiance data provide cloud properties that are of great significance for cloud-resolving models. Unlike MW and IR data, the radiance contributed by clouds could be easily extracted from the VIS observations because the VIS radiance data is much more sensitive to cloud variables than non-cloud variables.

Several studies have attempted to assimilate the SW radiance data directly (i.e. direct DA). Unlike indirect DA which assimilates the retrieved cloud parameters from SW radiance data, Direct DA critically depends on observation operators.

Several observation operators and relevant algorithms have been developed for the satellite VIS radiance DA. For example, 65 Vukicevic et al. (2004) mapped the model state variables to the equivalent radiance by an observation operator called the VIS and IR radiance measurements (VISIROO). **Later on**, Polkinghorne and Vukicevic (2011) **developed** the Spherical Harmonic Discrete Ordinate Method Plane Parallel for Data Assimilation (SHDOMPPDA), which solves radiative transfer processes by Discrete Ordinate Method (DOM) in Cartesian space while computing source functions using spherical harmonic series in spherical space. **Compared with** observation operators which solve source functions in Cartesian space, 70 SHDOMPPDA has an advantage of high computation efficiency. **To further speed up the computation**, Scheck et al. (2016a) developed a Method for Fast Satellite Image Synthesis (MFASIS), which is 2 ~ 4 orders of magnitude faster than the other DOM-based observation operators (Scheck et al., 2016b). Scheck et al. (2018) further improved MFASIS and reduced its errors due to three-dimensional (3D) radiative effects. MFASIS is one of the observation operators in the Radiative Transfer for TOVS (RTTOV). RTTOV contains several observation operators for satellite radiance DA (Saunders et al., 2018), 75 including DOM and the single-scattering method for SW radiative processes. These solvers could tackle cloud fraction, parallax correction, and many other critical aspects with respect to molecular absorption and scattering, underlying surface reflection, etc. (Saunders et al., 2018). Apart from these aforementioned observation operators, several machine learning-based observation operators and relevant methods (Scheck, 2021; Zhou et al., 2021) were developed and achieved high computation efficiency and accuracy for the VIS radiance simulations.

80 Another critical aspect of assimilating satellite VIS radiance data is **in the selection of DA algorithms**. There are two groups of mostly used DA approaches. The first is based on variational (VAR) methods. Vukicevic et al. (2004) assimilated GOES-9 VIS radiance data to the Regional Atmospheric Modeling System (RAMS) with a four-dimensional VAR (4DVAR) method and exhibited some positive effects on the short-term forecasting of a stratus cloud field. Similarly, Polkinghorne and Vukicevic (2011) assimilated the GOES-8 VIS and IR radiance data to RAMS with the 4DVAR system and also 85 **achieved some positive results**. The second is based on ensemble-based methods. The ensemble-based methods are remarkably stable for nonlinear systems and were used for cloud and precipitation studies by several researchers (Lei et al., 2015; Kurzrock et al, 2019). Schrötle et al. (2020) assimilated VIS and IR radiance data in an idealized Observing System Simulation Experiment (OSSE) framework using a Local Ensemble Transform Kalman Filter (LETKF). Their results indicated that assimilating VIS radiance data alone could improve the forecasting skills of the regional model, **COnsortium for Small-scale MOdeling (COSMO)**, and assimilating the VIS and IR radiance data collaboratively could further improve the forecasting skills. Their findings were further validated by Scheck et al. (2020) who concluded that assimilating the VIS radiance data of Spinning Enhanced Visible and Infrared Imager (SEVIRI) on METEOSAT could improve cloud and precipitation forecasts, and, meanwhile, **reduce the temperature and relative humidity forecast errors in most conditions**.

90 The VAR and ensemble-based approaches are complementary to each other. **The ensemble-based approaches generate the flow-dependent background error covariance matrices which can be used to leverage the VAR approaches**. Therefore, several hybrid approaches have been developed. Bauhner et al. (2013) evaluated an ensemble-VAR DA approach by assimilating the observations that were operationally assimilated in Environment Canada, and found it more skilful than the VAR method for the short- and mid-range forecasts over tropical and extra-tropical regions. Gao et al. (2013) developed a

hybrid Ensemble Kalman Filter (EnKF)-3DVAR method to assimilate radar data and found it outperforms 3DVAR or EnKF
100 in shortening the spin-up time of a supercell storm. In addition, hybrid methods are increasingly applied in the DA of satellite radiance data. Xu et al. (2016) assimilated the FY-3B satellite MW radiance data with the WRF hybrid ensemble/3DVAR and improved the forecasts of typhoons' track, intensities, and precipitation from 3DVAR. Similar results were also reported by Shen et al. (2020).

Nowadays, there are many community DA resources of the ensemble-based methods, such as the Data Assimilation
105 Research Testbed (DART, Anderson et al., 2009). DART supports several Numerical Weather Prediction (NWP) models including the Weather Research and Forecasting (WRF) model (Skamarock et al., 2008). Recently, WRF/DART incorporated the RTTOV radiative transfer package, facilitating the DA of satellite VIS to MW wavelengths radiance and enabling the DA of all-sky satellite SW radiance data. The Advanced Geostationary Radiation Imager (AGRI) on the geostationary FY-4A satellite launched in 2016, located over Asia, excels at high sampling frequency (5 min for intensive
110 observation and 15 min for operational observation) and high spatial resolution (0.5 ~ 2 km, depending on channels). Zhang et al. (2019) pointed out that AGRI provides great radiance measurements describing rapidly evolving and small- to meso-scale atmospheric systems. However, these data have not been assimilated in the operational NWP centres.

In this study, FY-4A/AGRI VIS radiance data were simulated in an OSSE framework and experiments of the VIS radiance DA were conducted using the WRF/DART-RTTOV system. We intended to answer the following three questions.
115 1) What are the advantages and limitations of assimilating the FY-4A VIS radiance for forecasting tropical storms? 2) How to specify the WRF/DART-RTTOV model settings and observations? 3) What needs to be considered for the real DA applications of FY-4A VIS radiance data? The result of this study is preliminary toward evaluating the WRF/DART-RTTOV system in assimilating all-sky FY-4A/AGRI VIS radiance data. It should be applicable to the DA of the upcoming FY-4B VIS radiance data as well because the designs of the AGRI payload for the FY-4A and -4B are similar. The remaining
120 manuscript is organized as follows. The models and experiment designs are introduced in Section 2. The impact of assimilating the FY-4A VIS radiance data on the analysis and first-guess forecasts of the tropical storm is discussed in Section 3. Finally, the conclusion and an outlook of future works are summarized in Section 4.

2. Models and experiment designs

The OSSE framework in this study consists of a nature run, a control run, a cluster of single observation experiments, and a
125 group of cycled DA experiments. The nature run was performed to generate a proxy true atmosphere of a tropical storm case. The DA experiments that assimilated the simulated FY-4A VIS radiance data were carried out to explore the impact of the FY-4A VIS radiance DA on the tropical storm forecast. A control run that excluded DA was performed for comparison. The OSSE was performed based on the tropical storm "Higos" in 2020.

On August 16, 2020, a tropical disturbance occurred over the north of Luzon, the Philippines. The system tracked
130 northwest toward the South China Sea, and intensified into a tropical storm on 19:00 August 17. The tropical storm was further developed into a typhoon system named Higos on 12:00 UTC, August 18. Higos landed on Zhuhai, Guangdong

province on 22:00 UTC, August 18, and weakened into a tropical depression on 12:00 UTC, August 19. This study focuses on the pre-landfall stage of the tropical storm (00:00 UTC ~ 12:00 UTC, August 18) in consideration that FY-4A VIS imagery is only available at daytime. During this period, the tropical storm had multi-layer and mixed-phase cloud structures, 135 which facilitates the evaluation of the abilities of assimilating VIS radiance data for these cloud structures.

2.1 Configurations of the WRF Mode

The WRF model domain settings were kept same for the nature run, control run, and DA experiments to avoid errors due to displacement of grids between the observation and simulations. The WRF model domain covers parts of the East Asia and

140 Western Pacific (Figure 1). The domain contains 151×177 horizontal grid boxes with a grid spacing of 15 km in the horizontal directions and 40 vertical levels, and the model top was set to 50 hPa. To avoid the disturbances over the regions close to the model domain boundaries, simulations within the inner rectangle of 131×157 horizontal grids are analysed.

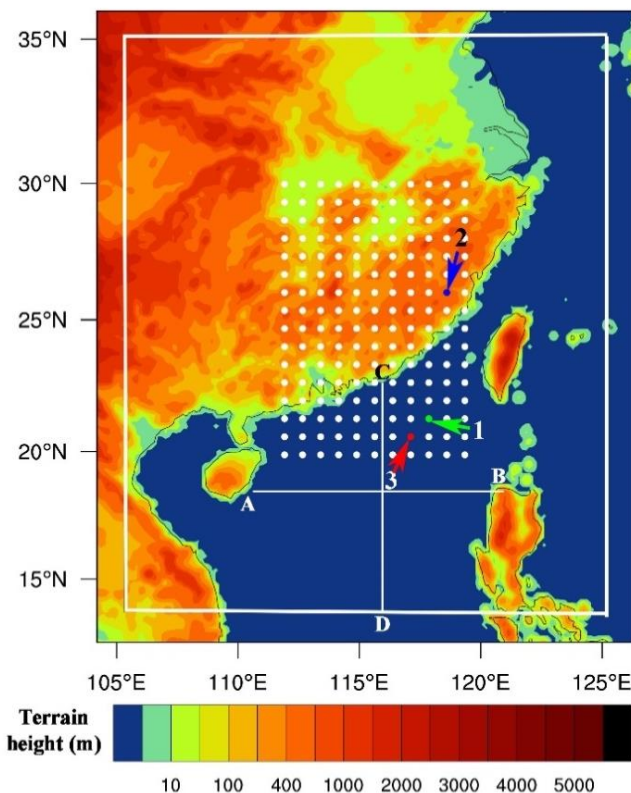


Figure 1. The WRF model domain with 15-km horizontal grid spacing. Only the observations within the inner white rectangle were assimilated and those close to the model domain boundaries were discarded. The white dots denote the locations that were used for single observation experiments (discussed in Section 2.3.2). Detailed discussions are given for points 1 (green), 2 (blue), and 3 (red) in the text. The two white lines, AB and CD, are for cross-section analyses.

145 For the nature run, the initial conditions (ICs) and lateral boundary conditions (LBCs) were extracted from the National Centers for Environmental Prediction (NCEP) Final (FNL) Operational Global Analysis data (with $1^\circ \times 1^\circ$ resolution,

available at <https://rda.ucar.edu/datasets/ds083.2/>). The WRF model configurations include the Thompson microphysical scheme (Thompson et al., 2008), the Tiedtke Cumulus Parameterization option (Tiedtke, 1989; Zhang et al., 2011), and the University of Washington (UW) planetary boundary layer scheme (Bretherton and Park, 2009). These are the optimal schemes for typhoon simulations over the Northwest Pacific Ocean as suggested by Di et al (2019). The other model configurations include the revised MM5 Monin-Obukhov surface layer scheme (Jiménez et al., 2012), the five layer thermal diffusion land surface scheme (Dudhia, 1996), and the Rapid Radiative Transfer Model for Global Climate Models (RRTMG) longwave and shortwave radiation schemes (Iacono et al., 2008). The Thompson microphysical scheme provides prognostic variables of liquid water particles including cloud water droplets and rain drops, and ice particles including ice crystals, snow, and graupel. The nature run was initialized with a cold start at 12:00 UTC 17 August 2020. To exclude a spin-up time of 14 hr, the WRF model simulations between 02:00 and 12:00 UTC, 18 August 2020 were used as a proxy true atmosphere of the tropical storm. The nature run captured the track and general properties of Higos. Synthetic observations of FY-4A VIS radiance were simulated with RTTOV which will be described in details in Section 2.2. The simulated VIS imagery (15 km \times 15 km resolution) was approximately equivalent to the superorbited 2km-resolution imagery (as those provided by FY-4A real observations) by averaging the 2 km \times 2 km imagery for every block of about 7 \times 7 pixels. Because the observation locations and model grid points are overlapped, the locations of the synthetic observations are directly assigned to the model grid points without interpolation during the DA processes.

For the cycled DA experiment, the ensemble size is set to 40 and the ICs and LBCs were extracted from the ERA5 hourly data at 0.25 \times 0.25 $^{\circ}$ resolution (available at <https://cds.climate.copernicus.eu/api/v2>). Perturbations, which were extracted based on the WRF 3DVAR system using a generic background error option with proper scaling, were added to the ICs. The scaling factors for the variance, horizontal length scale, and vertical length scale are set to 0.25, 1.0, and 1.5, respectively. To avoid discontinuities and poor results at the boundary, LBCs at each analysis time were updated based on the analysis and WRF lateral boundary conditions using an approach built in the DART *pert_wrf_bc* module. This is the reason why we choose the higher resolution LBCs, as will be done in real DA applications, for the DA experiments than for the nature run. The WRF model microphysics configurations are the same as the nature run. The ensemble members were initialized by a cold start at 00:00 UTC 18 August 2020. After a spin up of 2 hr, synthetic visible radiance observations were assimilated to the ensemble members from 02:00 to 09:00 UTC 18 August 2020. The time span corresponds to the daytime when VIS imagery is available. The ensemble members were advanced to 12:00 UTC. The updating frequency of the first-guess state variables was set according to different experiment designs summarized in Table 1. With these set ups, the effects of assimilating VIS imagery on the spin up of the WRF model and on the analysis and first-guess forecasts of the state variables including cloud and precipitation were explored. The model settings for the control run are the same as the cycled DA experiments, except that no observations were assimilated.

180 **2.2 Configurations of the RTTOV radiative transfer package**

Synthetic AGRI channel 2 radiance was simulated based on WRF outputs using the RTTOV radiative transfer package. The input parameters of RTTOV include cloud-related parameters (the vertical structures of liquid water mixing ratio, ice water mixing ratio, cloud water effective radius, cloud fraction, etc.), atmosphere profiles (the water vapour mixing ratio profile, temperature profile, etc.), surface properties (elevation, surface type, etc.), sun-satellite viewing geometries, etc. In the partly cloudy regions, the TOA radiance is a weighted average of the radiance for a clear sky and a cloudy sky. **The weight attached to the cloudy sky (i.e., the effective cloud fraction) was calculated as the vertically averaged cloud fraction weighted by the mixing ratio of hydrometeors (Geer et al., 2009).** It is noted that cloud fraction (CFC) parameterization in WRF model depends on relative humidity (RH), the saturation water vapour mixing ratio (q^*), and cloud water + ice mixing ratios (q_{l+i}) (Xu and Randall, 1996),

$$190 \quad \text{CFC} = \begin{cases} RH^p \left[1 - \exp \left(\frac{-\alpha q_{l+i}}{[(1-RH)q^*]\gamma} \right) \right], & \text{if } RH < 1 \\ 1, & \text{if } RH \geq 1 \end{cases} \quad (1)$$

where p , α , and γ are suggested to be 0.25, 100, and 0.49 separately.

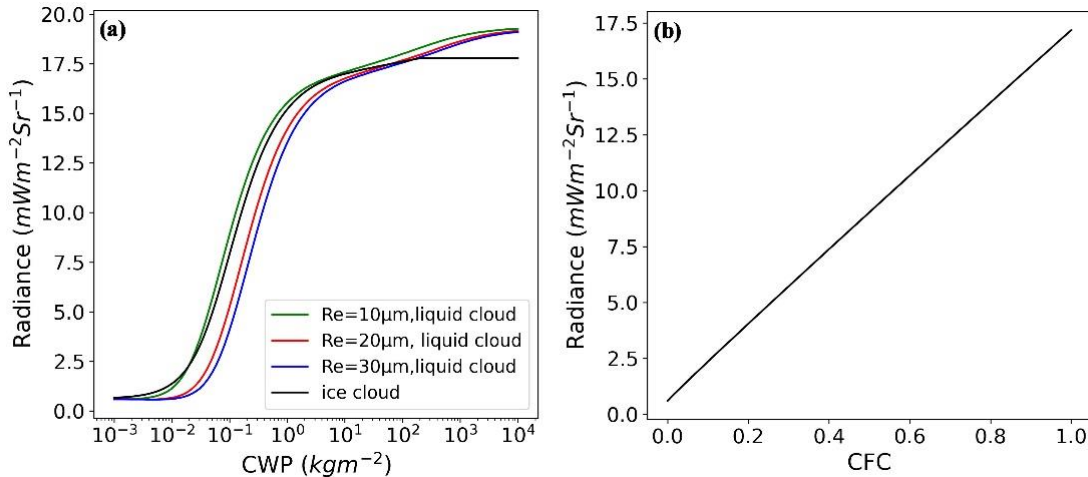
The solar zenith angle, solar azimuth angle, satellite viewing zenith angle, and satellite azimuth angle were calculated using the Python *astropy* library according to the UTC time and the FY-4A satellite position (104.7 °E). In addition, errors ranging from $1 \sim 4 \text{ mW m}^{-2} \text{ sr}^{-1}$ were assigned to the observations (Table 1). RTTOV includes the schemes considering different pre-defined cloud optical properties. For liquid water clouds, the “Deff” scheme where cloud optical properties are parameterized in terms of Re (Mayer and Kylling, 2005) was used. The cirrus scheme developed by Baren et al. (2014) was used to calculate ice cloud optical properties, which has no explicit dependence on ice particle size. Therefore, analyses of the results were simplified given that cloud variables were adjusted collectively but we do not have to analyse the effective radius of ice particles.

200 The radiative transfer processes were simulated by the DOM solver in RTTOV. The surface was treated as a specular reflector for downwelling emitted radiance. For land surface, the surface Bidirectional Reflectance Distribution Function (BRDF) was drawn from the land surface atlases (Vidot and Borbás, 2014; Vidot et al., 2018). For sea surface, BRDF was calculated with the JONSWAP (Hasselmann et al., 1973) solar sea BRDF model. The lay-to-space transmittance was computed by the v9 predictor on 54 levels (Matricardi, 2008). The downwelling atmospheric emission was computed using the linear-in-tau approximation for the Planck source term. Water vapour profiles were drawn from the WRF outputs. Other parameters not explicitly mentioned are set to the default values in DART/RTTOV.

Based on the above model configurations, the dependence of AGRI channel 2 radiance on the Cloud Water Path (CWP) and effective radius of cloud water droplet (Re) is presented in Figure 2. CWP denotes the vertically integrated cloud liquid and ice water mixing ratio in an atmospheric column, which is calculated by,

$$210 \quad \text{CWP} = \int_{P_s}^{P_t} \frac{1}{g} (Q_c + Q_i) dP \quad (2)$$

where P_s and P_t denote the surface and model top pressures. Q_c and Q_i are the liquid water mixing ratio (the sum of the mixing ratio of cloud droplet and rain) and ice water mixing ratio (the sum of the mixing ratio of ice, snow, and graupel), and g the gravitational acceleration (9.8 ms⁻²).



215 **Figure 2. Dependence of AGRI channel 2 radiance on (a) cloud water path (CWP) and effective radius (Re), and (b) cloud fraction (CFC) for CWP of 10 kg m^{-2} and Re of $15 \mu\text{m}$. The simulation was performed with the “Deff” scheme for liquid water cloud optical properties and the Baren et al. (2014) scheme for cirrus optical properties. The solar zenith angle, viewing zenith angle, and relative azimuth angle were set to 25° , 40° , and 135° , respectively.**

220 The curvature properties in Figure 2 indicate a non-linear relationship between the observation (radiance) and cloud parameters (CWP and Re). The variation of the radiance-CWP functions with different effective radii become smaller as Re increases. For Re larger than $30 \mu\text{m}$, the radiance-CWP functions almost do not change with effective radii. Because raindrops are several orders larger than cloud droplets, the effective radius of cloud droplets is sufficient to describe the radiative transfer processes for the clouds where cloud droplets and raindrops coexist. As a result, Re in the following discussion explicitly denotes the effective radius of cloud droplets, which corresponds to the WRF state variable
225 “RE_CLOUD”.

2.3 DA experiment design and DART configurations

2.3.1 DART filters

230 DART was configured to employ the Ensemble Adjustment Kalman Filter (EAKF, Anderson, 2001) and the Rank Histogram Filter (RHF, Anderson, 2010) for this study. EAKF and RHF are two variants of the deterministic filters. Therefore, no perturbations were added to the observations. EAKF is a serial ensemble DA algorithm and the observations are assimilated as scalars. The model state variable \mathbf{x}_m is updated by Equation (3) (Anderson, 2001),

$$x'_m = x_m + \Delta x_{m,n}, \quad m = 1, \dots, M, n = 1, \dots, N \quad (3)$$

where \mathbf{x}_m denotes the m^{th} state variable, \mathbf{x}'_m the updated value of \mathbf{x}_m , and $\Delta\mathbf{x}_{m,n}$ the state variable increment for the m^{th} state variable due to the n^{th} observation. $\Delta\mathbf{x}_{m,n}$ is calculated by Equation (4),

$$235 \quad \Delta\mathbf{x}_{m,n} = (\sigma_{p,m}/\sigma_p^2)\Delta y_n, \quad m = 1, \dots, M, n = 1, \dots, N \quad (4)$$

where the subscript “ p ” stands for the prior estimate (i.e., the first guess), $\sigma_{p,m}$ is the first-guess sample error covariance between the observation and the m^{th} state variable \mathbf{x}_m , and σ_p^2 the first-guess sample error variance of the observed variable. Δy_n is the observation increment for the n^{th} ensemble, which is calculated by the following equation,

$$\Delta y_n = (y_n^p - \bar{y}_p)(\sigma_u/\sigma_p) + \bar{y}_u - y_n^p, \quad n = 1, \dots, N \quad (5)$$

240 where y_n^p denotes the first guess of the observed variable for the n^{th} ensemble, \bar{y}_p the ensemble mean of the first guess of the observed variable, \bar{y}_u the ensemble mean of the posterior estimate (i.e., the analysis) of the observed variable, σ_u the updated standard deviation of σ_p . \bar{y}_u and σ_u are calculated by Equations (6) ~ (7).

$$\bar{y}_u = \frac{\sigma_o^2}{\sigma_o^2 + \sigma_p^2} \bar{y}_p + \frac{\sigma_p^2}{\sigma_o^2 + \sigma_p^2} y_o \quad (6)$$

$$\sigma_u = \sqrt{\frac{\sigma_o \sigma_p}{\sigma_o^2 + \sigma_p^2}} \quad (7)$$

245 where y_o and σ_o denote the observation and its corresponding observational error standard deviation.

Anderson (2007; 2009) promoted a spatially varying state-space adaptive covariance inflation to the first-guess state to increase the prior ensemble spread. The same option was adopted in this study and also several other papers (Lei et al., 2015; Kurzrock et al., 2019). The adaptive inflation uses 1.0, 0.6, and 0.9 as the initial value, fixed standard deviation, and damping settings, respectively. The sampling error due to the use of the limited ensemble size was corrected by the method 250 developed by Anderson (2012). Since observations like satellite VIS radiance data do not have a specific single vertical location, no vertical localization was used in this study.

The RHF produces a posterior ensemble based on a continuous approximation of the prior Probability Density Function (PDF) and a piecewise linear representation of the likelihood. The prior PDF is approximated by a rank histogram which has a piecewise constant between two ensemble members and follows Gaussian distributions beyond the lower and upper bounds 255 of the ensemble members. The posterior distribution is calculated by the Bayes Theorem, and the state variable is updated by searching the appropriate position in the state variable space which partitions the posterior distribution to unity probability for each ensemble member. The prior PDF does not have to respect the Gaussian form for RHF. Therefore, the method is declared to be more suitable for non-Gaussian problems. Details on this algorithm can be found in Anderson (2010).

2.3.2 Single observation experiments

260 With the OSSE setups, a set of single observation experiments were performed by employing EAKF to assimilate the VIS
radiance data. The single observation experiments assimilate an observation at a given pixel, and the adjustment of state
variables in the column at a targeting pixel is only caused by assimilating the one observation. This is convenient to evaluate
the basic functionality of assimilating VIS radiance data. The potentials, inabilities and ambiguities of assimilating VIS
radiance data were discussed herein. The single observation experiments were performed at 02:00 UTC 18 August 2020, and
265 no forecast was carried out. The affected cloud variables include Qc, Qi, Re, CFC, and the non-cloud variables including
water vapour mixing ratio (Q), perturbation potential temperature (T), and the x- and y-wind components (U and V).

270 The single observation experiments were performed for the most inner parts of the satellite imagery to avoid
disturbances near boundaries. The observations at 02:00 UTC were thinned by selecting every six pixels to make sure that
the selected observations are far from each other. This resulted in 176 points shown in Figure 1. By setting a localization
distance of 15 km, assimilating the VIS radiance at a pixel would not influence the state variables at the surrounding pixels.
Therefore, we performed a cluster of 176 single observation experiments in one DA cycle to save computational cost, similar
to Scheck et al. (2020). Amongst the 176 selected pixels, special focuses were given to the three coloured points, which were
designed to illustrate the ambiguities related to cloud layered structures and cloud phases and to illustrate the limitations due
to the non-Gaussian and non-linear problems.

275 2.3.3 Cycled DA experiments

Fourteen cycled DA experiments were performed to evaluate the influences of different model settings and observation
pre-processing on the analysis and forecast with VIS radiance DA. The purpose of the cycled DA experiments is to reveal
the forecast quality and growth of the forecasting errors during assimilating satellite VIS radiance data, and to provide some
guidance on the use of WRF/DART-RTTOV and an outlook to the future applications. The experiment setups cover the tests
280 of different filter algorithms, cycling intervals, cycling variables, outlier threshold values, observation errors, and
observations with or without data-thinning. The outlier threshold value for the observation is a pre-defined threshold for
rejecting an observation depending on its distance from the ensemble mean of the first guess. If the distance is more than N
(the predefined outlier threshold value) standard deviations from the square root of the sum of the first-guess ensemble and
observation error variance, the observation is rejected. A description of the experiment designs are summarized in Table 1.

285 Comparison between Exp-01 ~ Exp-03 and Exp-4~Exp-06 groups was designed to reveal the pros and cons of EAKF
and RHF on the WRF analysis and forecast. Comparison between Exp-01 ~ Exp-02 and Exp-07 ~ Exp-08 groups was
designed to reveal the influences of updating the thermal and dynamic variables. Comparison between Exp-03, Exp-09, and
Exp-10 was designed to reveal the influences of the observation errors. Comparison between Exp-01 ~ Exp-03 and Exp-11~
Exp-13 groups was designed to reveal the influences of the outlier threshold values. Finally, comparison between Exp-10
290 and Exp-14 was designed to reveal the influences of observation thinning.

Table 1. Parameter settings for the cycled data assimilation experiments. x_{cloud} denotes the WRF cloud variables including cloud fraction (CLDFRA), the mixing ratio of cloud droplet (QCLOUD), rain (QRAIN), ice (QICE), snow (QSNOW), graupel (QGRAUP), the effective radius of cloud water droplet (RE_CLOUD), and the effective radius of cloud ice droplet (RE_ICE). x_{atmos} denotes the WRF non-cloud variables including water vapour mixing ratio (QVAPOR), water vapour mixing ratio at 2m height (Q2), x-, y-, and z-wind components (U, V, W), x- and y-wind components at 10 m height (U10 and V10), temperature at 2 m height (T2), perturbation geopotential (PH), perturbation potential temperature (T), perturbation dry air mass in column (MU), and surface pressure (PSFC).

DA experiments	Thinning length	Localization distance	Filter algorithm	Cycling interval	Cycling variables	Outlier threshold	Observation error
Exp-01	—	15 km	EAKF	10 min	$x_{\text{cloud}} + x_{\text{atmos}}$	3	$1 \text{ mW m}^{-2} \text{ Sr}^{-1}$
Exp-02	—	15 km	EAKF	1 hr	$x_{\text{cloud}} + x_{\text{atmos}}$	3	$1 \text{ mW m}^{-2} \text{ Sr}^{-1}$
Exp-03	—	15 km	EAKF	3 hr	$x_{\text{cloud}} + x_{\text{atmos}}$	3	$1 \text{ mW m}^{-2} \text{ Sr}^{-1}$
Exp-04	—	15 km	RHF	10 min	$x_{\text{cloud}} + x_{\text{atmos}}$	3	$1 \text{ mW m}^{-2} \text{ Sr}^{-1}$
Exp-05	—	15 km	RHF	1 hr	$x_{\text{cloud}} + x_{\text{atmos}}$	3	$1 \text{ mW m}^{-2} \text{ Sr}^{-1}$
Exp-06	—	15 km	RHF	3 hr	$x_{\text{cloud}} + x_{\text{atmos}}$	3	$1 \text{ mW m}^{-2} \text{ Sr}^{-1}$
Exp-07	—	15 km	EAKF	10 min	x_{cloud}	3	$1 \text{ mW m}^{-2} \text{ Sr}^{-1}$
Exp-08	—	15 km	EAKF	1 hr	x_{cloud}	3	$1 \text{ mW m}^{-2} \text{ Sr}^{-1}$
Exp-09	—	15 km	EAKF	3 hr	$x_{\text{cloud}} + x_{\text{atmos}}$	3	$2 \text{ mW m}^{-2} \text{ Sr}^{-1}$
Exp-10	—	15 km	EAKF	3 hr	$x_{\text{cloud}} + x_{\text{atmos}}$	3	$4 \text{ mW m}^{-2} \text{ Sr}^{-1}$
Exp-11	—	15 km	EAKF	10 min	$x_{\text{cloud}} + x_{\text{atmos}}$	6	$1 \text{ mW m}^{-2} \text{ Sr}^{-1}$
Exp-12	—	15 km	EAKF	1 hr	$x_{\text{cloud}} + x_{\text{atmos}}$	6	$1 \text{ mW m}^{-2} \text{ Sr}^{-1}$
Exp-13	—	15 km	EAKF	3 hr	$x_{\text{cloud}} + x_{\text{atmos}}$	6	$1 \text{ mW m}^{-2} \text{ Sr}^{-1}$
Exp-14	60 km	60 km	EAKF	3 hr	$x_{\text{cloud}} + x_{\text{atmos}}$	3	$1 \text{ mW m}^{-2} \text{ Sr}^{-1}$

2.4 Metrics of simulation errors

Root Mean Square Error (RMSE) and Mean Absolute Error (MAE) are two of the most used metrics to assess the weather simulation errors (Kurzrock et al., 2019). RMSE is much more sensitive to extremely large errors than MAE. For satellite VIS radiance DA, some extremely large analysis increments of CWP were rarely expected (details provided in Section 3), implying that the difference of RMSE between the first guess and the analysis was not as distinct as MAE. Thus, MAE is used to measure the difference between the simulated CWP and the theoretical true CWP (derived from the nature run).

MAE is calculated by the following formula,

$$305 \quad \text{MAE} = \frac{1}{n_x n_y} \sum_{i,j} \text{abs}(x_{i,j}^{\text{sim}} - x_{i,j}^{\text{obs}}) \quad (8)$$

where $x_{i,j}^{\text{sim}}$ ($x_{i,j}^{\text{obs}}$) denotes the simulated (true) CWP at the i^{th} (in the zonal direction) and j^{th} (in the meridional direction) model grid. n_x and n_y denote the number of pixels in zonal and meridional directions of the relevant model domains.

310 Fraction skill score (FSS) was developed to measure the accuracy of a spatially inhomogeneous variables on a certain spatial scale. Therefore, it can mitigate the “double-penalty” problem (Mittermaier et al., 2013) for small spatial shifts of interested features. FSS is calculated by the following formula,

$$FSS = 1 - \frac{\frac{1}{m_x m_y} \sum_{i,j} (p_{i,j}^{obs} - p_{i,j}^{sim})^2}{\frac{1}{m_x m_y} [\sum_{i,j} p_{i,j}^{obs} + \sum_{i,j} p_{i,j}^{sim}]} \quad (9)$$

where $p_{i,j}^{obs}$ denotes the cloud fraction within a subdomain covering 3×3 model grids. m_x and m_y denote the dimensions of subdomains in the zonal and meridional directions.

For precipitation simulation evaluation, Threat Score (TS) is used. TS is computed as,

$$315 \quad TS = \frac{H}{F+M+H} \quad (10)$$

where H denotes the number of pixels with the correct representation of precipitation (hits), F denotes the number of pixels where simulation indicates precipitation while the true state indicates non-precipitation (false alarms), and M denotes the number of pixels where simulation indicates non-precipitation while the true state indicates precipitation (under predictions).

320 Following Scheck et al. (2020), we also use the Mean Profile Error (MPE, ε) to assess the error of model state with respect to the nature run. If the difference between the MAE of the analysis (ε_{pos}) and that of the first guess (ε_{pri}), calculated as $\delta\varepsilon = \varepsilon_{pos} - \varepsilon_{pri}$, is negative, positive impact is generated by the DA procedure, and vice versa.

3. Results

3.1 Single observation experiments

325 The results discussed herein correspond to the OSSE setups described in Section 2.3.2. Only the ensemble mean of the first guess and analysis of state variables were discussed. We focused on three cases. 1) In both state variable (or a diagnosed parameter such as CWP) and observation spaces, the analysis is within the range bounded by the first guess and the truth; 2) The analysis is within the first guess and the truth in the observation space but not in the state variable space. This case is associated with the spurious covariance and non-linear properties of the forward operator; 3) The analysis is beyond the first 330 guess and the truth in both observation space and state variable space, which is closely related to the non-Gaussian properties of the prior PDF. The results including the three cases are shown in Figure 3.

Assimilating VIS radiance data generated trivial impact on the non-cloud variables including x- and y-wind components (U and V in Figure 3(a)), temperature and water vapour mixing ratio (T and Q in Figure 3(b)). From the perspective of radiative transfer, the VIS radiance is insensitive to U and V at the analysis time. Therefore, the adjustment in observation space should not influence U and V. In addition, the VIS radiance is closely related to CFC (Figure 2(b)), an implicit relationship between the VIS radiance and RH could be expected because the parameterization of CFC involves water vapor (Equation (1)). The VIS radiance is positively related to CFC. However, given that RH depends not only on Q, but also on T

and pressure, spurious covariance between the VIS radiance and Q/T may be generated due to the ensemble spread of Q/T. Note that different Q/T for the ensemble members would blur the relationship between VIS radiance and Q/T. Therefore, 340 only neutral **impact** on Q and T was revealed for the single observation experiments.

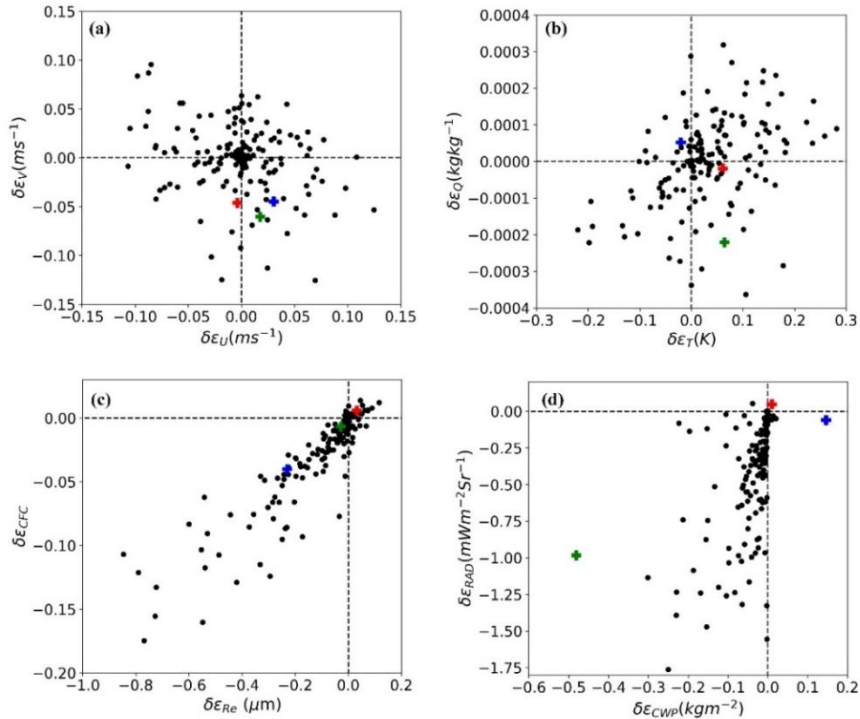


Figure 3. Differences of the Mean Profile Error (MPE) between the ensemble mean of the first guess and analysis, denoted as $\delta\epsilon_X = X_{MPE, pos} - X_{MPE, pri}$, where X denotes a state variable or a diagnosed parameter, and pos and pri the analysis and first guess, respectively. The variables include (a) the x- and y-wind components (U and V), (b) the perturbation potential temperature (T) and water vapour mixing ratio (Q), (c) the cloud fraction (CFC) and effective radius (Re), and (d) cloud water path (CWP) and 345 radiance (RAD). The plus signs in green, blue, and red colours correspond to points 1, 2, and 3 in Figure 1.

Assimilating VIS radiance data improved the ensemble mean of Re, CFC, CWP, and VIS radiance for most points in Figure 3(c) and 3(d). Take Point 1 marked in Figure 1 as an example for case 1. The profiles of the ensemble mean of cloud and non-cloud variables for the **first guess and analysis** are shown in Figure 4. Point 1 corresponds to a single ice cloud layer 350 between 400 ~ 200 hPa with a CWP of 0.01 kg m^{-2} and a top-of-atmosphere (TOA) radiance of $3.63 \text{ mW m}^{-2} \text{ Sr}^{-1}$ for the nature run. The **first guess** features a two-layer mixed-phase cloud with a false alarm liquid water cloud layer below 500 hPa. The ensemble mean first-guess CWP and the equivalent VIS radiance are 1.33 kg m^{-2} and $7.29 \text{ mW m}^{-2} \text{ Sr}^{-1}$, respectively. After assimilating the satellite VIS radiance data, the **first guess** was drawn toward the nature run both in the observation 355 space, with a decreased ensemble mean radiance of $6.40 \text{ mW m}^{-2} \text{ Sr}^{-1}$, and in CWP, with a decreased ensemble mean CWP of 0.85 kg m^{-2} . As a result, Qc, Qi, CFC, and Re were adjusted collaboratively toward the nature run.

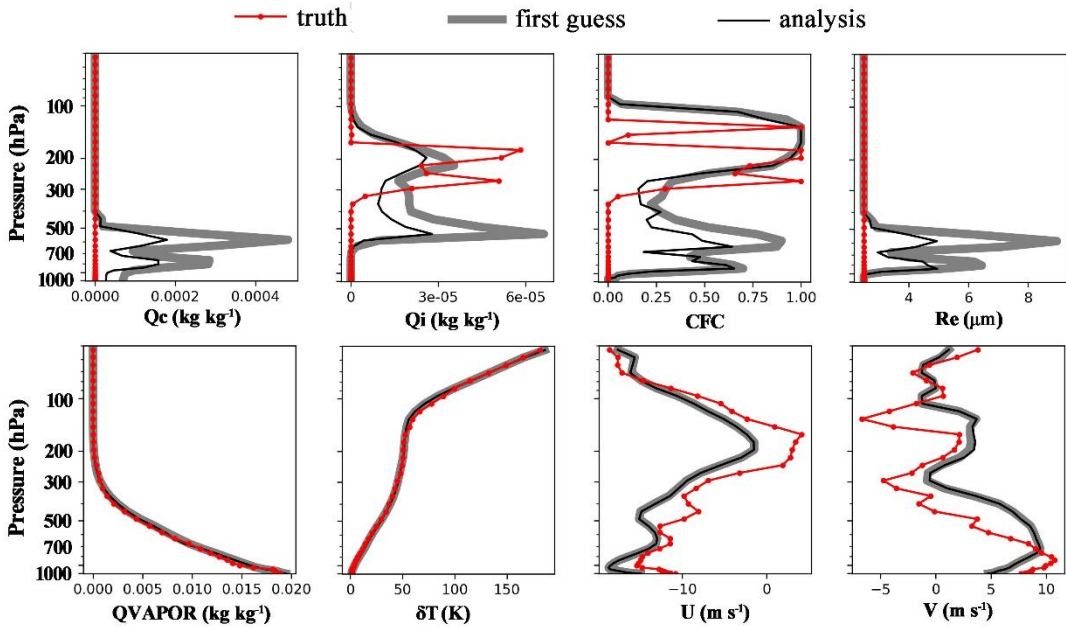


Figure 4. The vertical profiles of state variables for the nature run (theoretical truth), the **first guess** and **analysis** (ensemble mean). Qc denotes the liquid water mixing ratio, Qi the ice water mixing ratio, CFC the cloud fraction, Re the effective radius of liquid water droplets, QVAPOR the water vapour mixing ratio, δT the perturbation potential temperature, U and V the x- and y-wind components.

360

365

370

Since the simulated VIS radiance observation is not sensitive to cloud vertical structures but to the accumulated cloud water/ice mass, assimilating the VIS radiance observation could not reduce cloud vertical location errors. In addition, it could not remove the false alarm liquid clouds produced by the spurious covariance between the VIS radiances and liquid water clouds in the background. According to Equation (4), the analysis increment of each state variable is linearly related to its covariance with observations. Therefore, the vertical structures and hydrometeor phases of the **analysis** are mainly determined by those of the **first guess**. A larger **first guess** of the state variable would generate larger covariance, and a larger adjustment to the **first guess** would be expected. Because the ensemble mean of the **first-guess** Qc and Qi were larger in the lower layer (≥ 400 hPa), the adjustment of Qc/Qi were much more distinct for the lower layer than the upper layer (≤ 300 hPa). Similar results were also found for Re except that larger liquid water particles occurred in the middle layer (~ 600 hPa) and smaller liquid water particles occurred in the lower layer (~ 800 hPa). The covariance between CFC and the synthetic observation is zero in the upper layer (≤ 200 hPa) because CFC is almost a constant of 1 for all ensemble members (the ensemble spread of CFC is zero). Compared with the cloud variables, the non-cloud variables remain almost unchanged after the DA.

375

Case 2 is used to illustrate that positive **impact** on VIS radiance does not ensure positive **impact** on CWP. Take Point 2 in Figure 1 as an example, the theoretical truth, the ensemble mean of the first guess and the analysis of radiance/CWP are $8.59 \text{ mWm}^{-2}\text{Sr}^{-1}/0.17 \text{ kgm}^{-2}$, $7.94 \text{ mWm}^{-2}\text{Sr}^{-1}/2.50 \text{ kgm}^{-2}$, and $8.00 \text{ mWm}^{-2}\text{Sr}^{-1}/2.65 \text{ kgm}^{-2}$, respectively. That is to say, the

analysis of CWP is beyond the range bounded by the first guess and the truth. This is partly due to the non-linear relationship between CWP and VIS radiance. To elaborate this problem, we calculated the ensemble mean with Formula (4) and substituting \bar{y}_u in Formula (6) would get the following formula,

380
$$\overline{\Delta x_m} = \frac{\sigma_{p,m}}{\sigma_0^2 + \sigma_p^2} R_{inc} \quad (11)$$

where $\overline{\Delta x_m}$ denotes the ensemble mean of the m^{th} state variable increment, R_{inc} the ensemble mean radiance increment, which is calculated by the following formula,

$$R_{inc} = y_o - \bar{y}_p \quad (12)$$

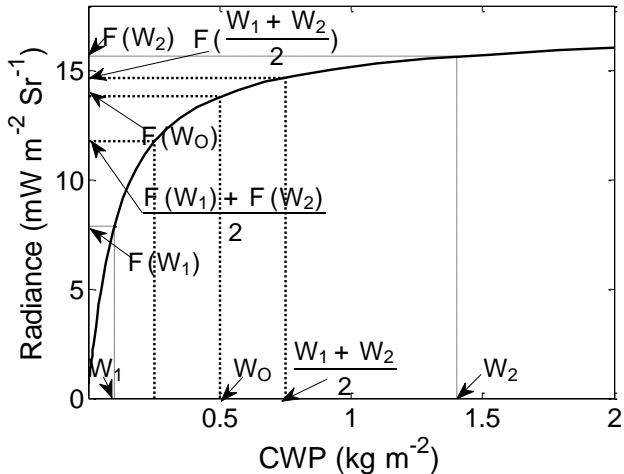
Considering a simplified case with just 2 ensemble members, the ensemble mean observation increment is calculated by 385 the following formula,

$$R_{inc} = F(W_o) - \frac{F(W_1) + F(W_2)}{2} \quad (13)$$

where W_o denotes the observed CWP and F denotes the forward operator. W_1 and W_2 represent CWP of the two ensemble members. However, considering the relationship between CWP and the VIS radiance, the theoretical true observation increment should be,

390
$$R_{inc}^t = F(W_o) - F(\bar{W}), \bar{W} = \frac{W_1 + W_2}{2} \quad (14)$$

As indicated by Figure 4, R_{inc} is larger than R_{inc}^t . That is, the ensemble mean observation increment was overestimated by Equation (14), leading to an over-estimated ensemble mean of the analysis of CWP.



395 **Figure 5. Illustration of the nonlinear effects of the observation operator on the calculation of radiance increments with 2 ensemble members. F denotes the observation operator, W_1 and W_2 denote cloud water path (CWP) for the 1st and 2nd ensemble member, W_o denotes the observed CWP.**

Case 3 is to show that some negative **impact** could be generated in the observation space in some conditions. Take Point 3 in Figure 1 as an example, the ensemble mean radiance ($2.51 \text{ mWm}^{-2}\text{Sr}^{-1}$) of the analysis is beyond the range bounded by the ensemble mean of the first guess ($2.56 \text{ mWm}^{-2}\text{Sr}^{-1}$) and the true radiance ($3.41 \text{ mWm}^{-2}\text{Sr}^{-1}$). The EAKF algorithm 400 assumes that the prior PDF, $p(x)$, of **the equivalent observations** and model state variables (or the diagnosed variable such as CWP in this study) confirms to Gaussian **functions**. To see how well the assumption was respected, $p(x)$ of **radiance and CWP is** presented in Figure 6. It shows **non-Gaussian prior PDFs**. Several studies concluded that the non-Gaussian properties negatively affect the performance of ensemble methods (Lawson & Hansen, 2004; Lei et al., 2010). Therefore, we 405 **tentatively** ascribe the negative **impact** in the observation space partly to the non-Gaussian properties of $p(x)$. Accordingly, **DA** experiments using RHF, which is not bound by the assumption of Gaussian, were added to the cycled **DA** experiments in comparison with EAKF.

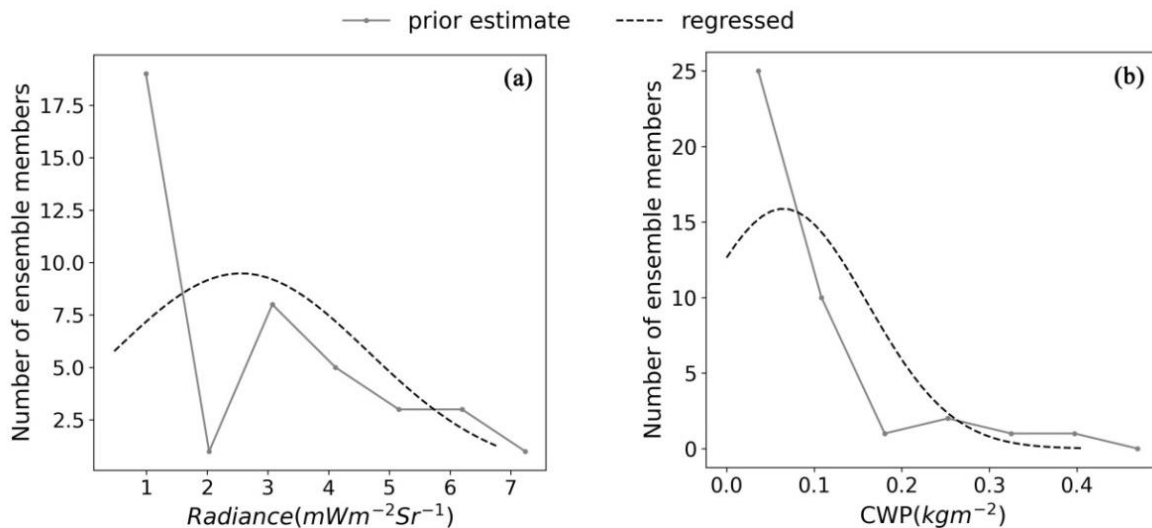


Figure 6. The first-guess Probability Density Functions (PDFs) of (a) equivalent visible radiance and (b) the cloud water path (CWP). The PDFs were estimated from the 40 prior ensembles for Point 3 (red dot) in Figure 1.

410 3.2 Cycled DA experiments

The results in this section correspond to the OSSE setups described in Section 2.3.3. The main focuses are the **impact** of the VIS radiance **DA** on the analysis and first-guess forecast of CWP, cloud coverage, non-cloud state variables, and precipitation.

3.2.1 Impact on CWP and cloud coverage

415 The time evolution of CWP for the nature run, control run, and the first-guess forecast and the analysis of CWP for Exp-01 are presented in Figure 7.

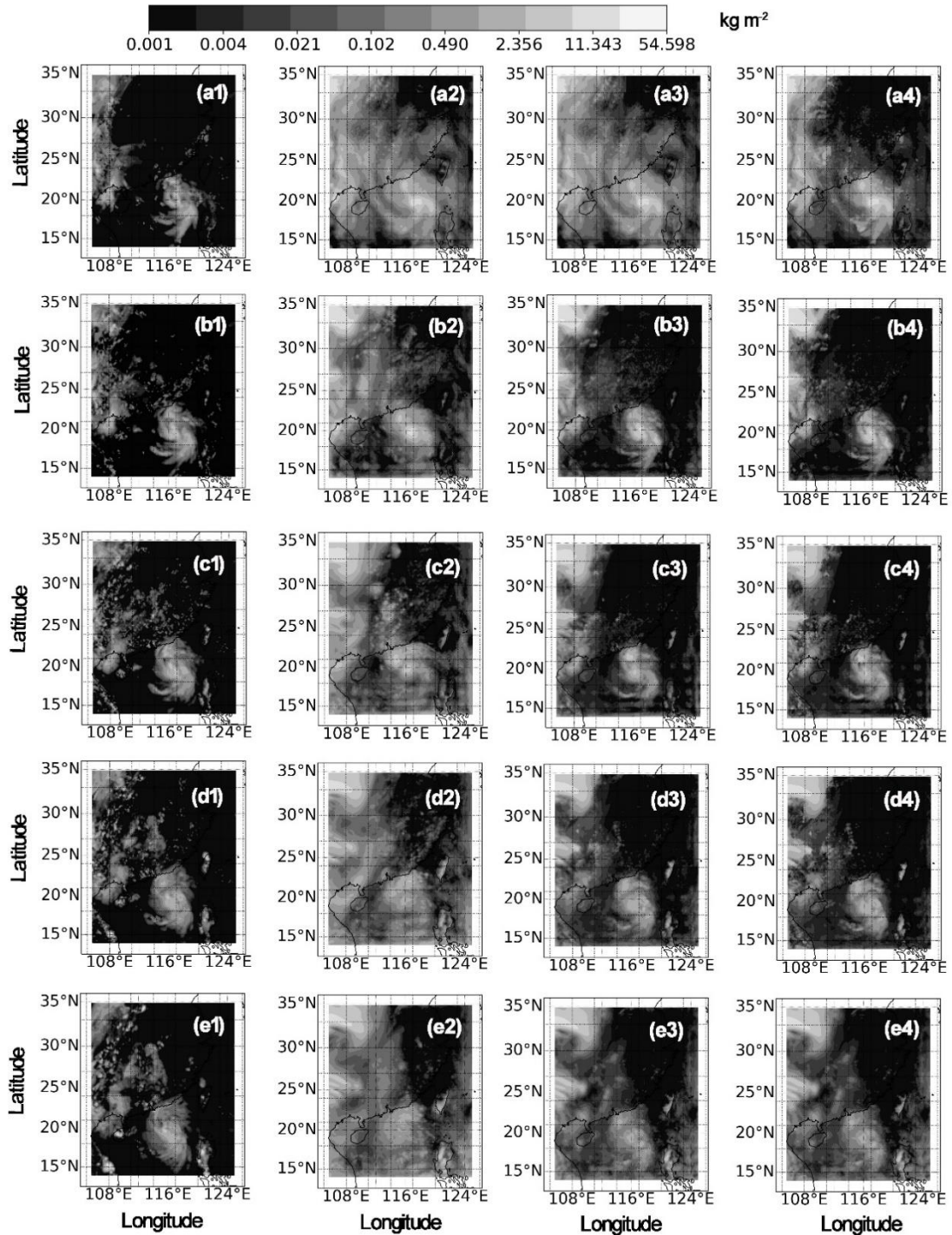
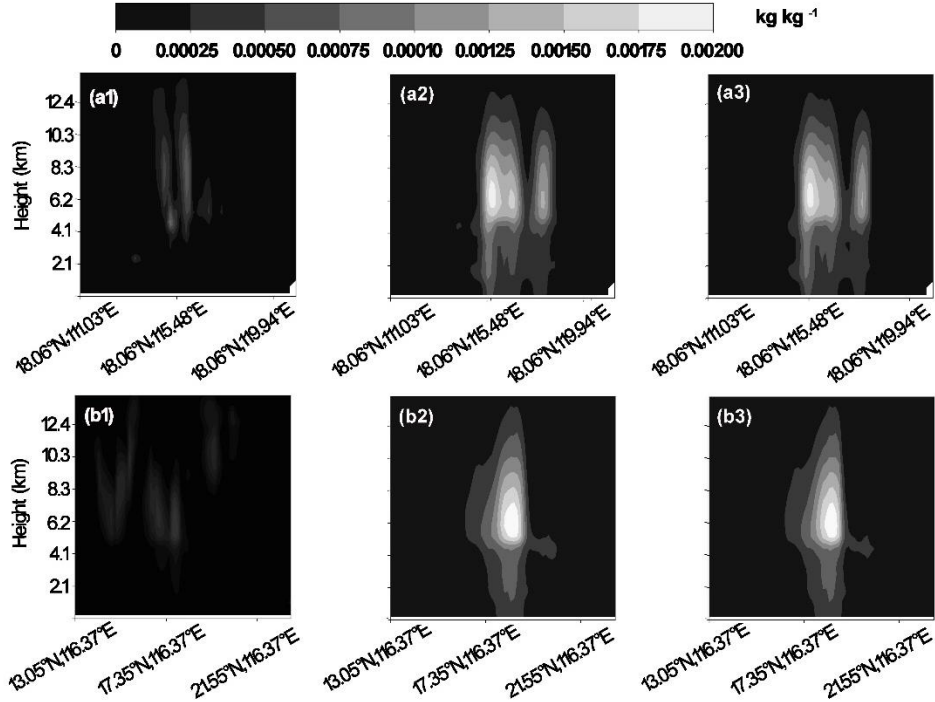


Figure 7. The time evolution of cloud water path (CWP) for the nature run (column 1), control run (column 2), first-guess forecast (column 3), and analysis (column 4) of Exp-01. From top to bottom, the row panels correspond to 02:00, 04:00, 06:00, 08:00, and 10:00 UTC on 18 August 2020.

The results indicate distinct differences between the first guess and the analysis of CWP on 02:00 UTC, 18 August 2020 (Figure 7(a3)-7(a4)). After assimilating the VIS radiance data, the horizontal distribution of the ensemble mean first-guess CWP is quite similar to that of the analysis. An extremely large analysis increment of CWP was rarely expected as mentioned in Section 2.4. The resemblance between the cycled DA experiments and the nature run also indicates the improvements on the analysis and the first-guess forecast of CWP and cloud coverage. Compared with the control run, assimilating the VIS radiance data clearly suppressed the false alarm clouds. However, DA of VIS radiance could not generate clouds which were under-predicted. The inability to correct the underprediction was illustrated with a cross-section analysis shown in Figure 8.



430 **Figure 8. The x-press cross section of the cloud water and ice mixing ratios of Exp-01 at 02:00 UTC, 18 August 2020 for the AB (the upper panel) and CD (the lower panel) lines shown in Figure 1. From left to right, the column panels correspond to the nature run, the ensemble mean of the first guess, and the ensemble mean of the analysis, respectively.**

Assimilating VIS radiance data did not improve the underprediction of the cloud distributions in vertical and horizontal directions. In the vertical direction, a single layer cloud was presented between 4 and 12 km height in the nature run (Figure 435 8(a1) and 8(b1)). However, clouds were presented between 0 and 12 km height in the first guess (Figure 8(a2) and 8(b2)). After the DA, Q_c/Q_i was decreased but the clouds below 4 km height were not removed (Figure 8(a3) ~ 8(b3)). In the horizontal direction, a thin-layer cloud was presented between $14^{\circ}\text{N} \sim 16^{\circ}\text{N}$ in the nature run (Figure 8 (b1)). This cloud fragment was not simulated by the first-guess atmosphere state (Figure 8 (b2)), nor was it regenerated after assimilating the VIS radiance data (Figure 8(b3)). Therefore, assimilating the VIS radiance would not generate cloud hydrometers for the

440 region with clear sky in the first guess because there is only zero spread of cloud variables from the unrepresentative background error covariance.

Quantitative analyses of CWP and CFC indicated improved analysis and first-guess forecasts for the cycled DA experiments. The results are varying with filter algorithms, cycling variables, outlier thresholds, observation errors, and observations with or without thinning, which were discussed in the following.

445 *a. Influences of filter algorithms*

To evaluate the performances of different filters on the analysis and first-guess forecast of cloud variables, quantitative analyses of FSS and MAE of the ensemble mean CWP for Exp-01 ~ Exp-03 (EAKF) and Exp-04 ~ Exp-06 (RHF) are presented in Figure 9. In general, the performance of RHF is comparable to or slightly better than EAKF. At some analysis times before 03:00 UTC, the FSS of CWP for the analysis is larger for Exp-01 than for Exp-04, but the first-guess FSS at the 450 next analysis time is larger for Exp-04 than Exp-01. Similar results were found for the 1 hr and 3 hr first-guess forecasts. These results imply that better analyses do not always ensure better forecasts.

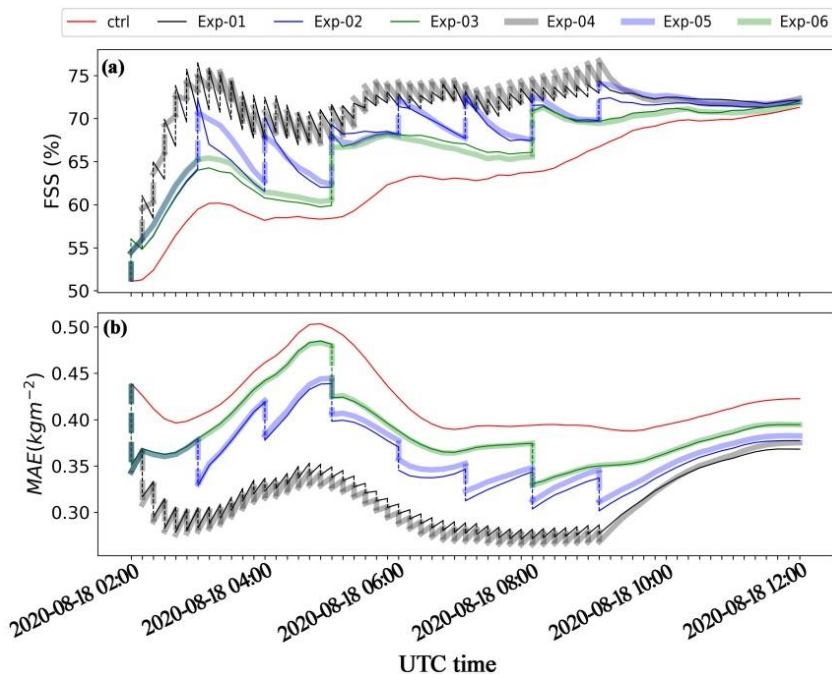


Figure 9. The time evolution of (a) FSS and (b) MAE of the ensemble mean of the first-guess forecast and analysis of CWP for the cycled DA experiments which are designed to illustrate the sensitivity to filter algorithms.

455 Unlike EAKF that assumes a Gaussian prior PDF, RHF does not. However, the performance of RHF is also subject to the sampling errors due to limited ensemble members and other factors as indicated by Anderson (2010). Therefore, only comparable or slightly better analysis and first-guess estimates were revealed for RHF than EAKF. In addition, updating the state variables by RHF is at a sacrifice of more computational cost. For the DA of 20567 observations in one DA cycle at a

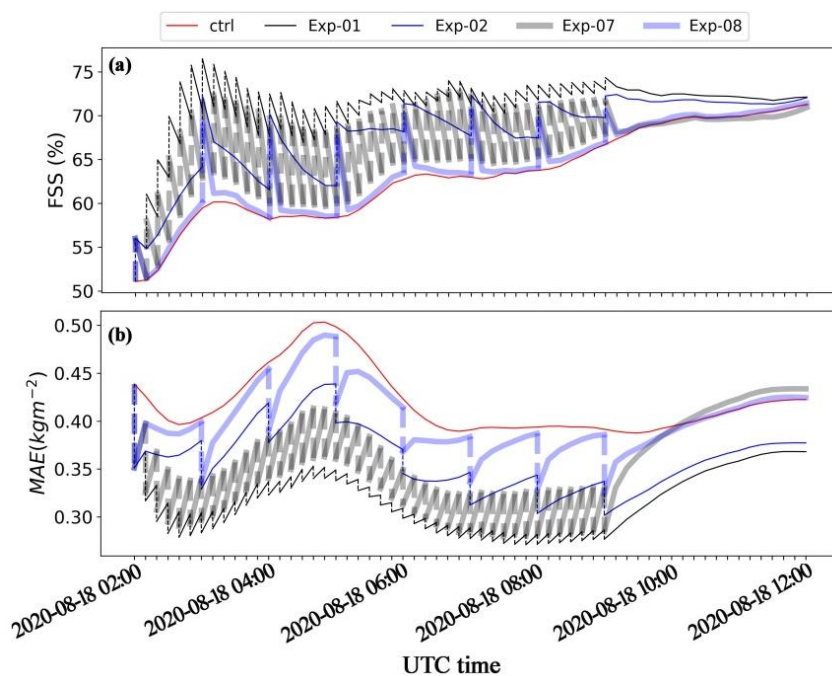
Linux cluster equipped with a 2.20 GHz Xeon Silver 4214 CPU with 12 cores, the elapsed CPU time is 775 s and 440 s for

460 the RHF and EAKF methods, respectively.

b. Influences of cycling variables

The single observation experiments indicate that assimilating VIS radiance data only generated trivial **impact** on non-cloud variables at 02:00 UTC, 18 August 2020. However, the non-cloud variables are an important part of a cycling **DA** system. To explore the **impact** of including or excluding the updated non-cloud parameters in the ensemble cycles, FSS and

465 MAE of the 10 min and 1 hr first-guess forecast and analysis of the ensemble mean CWP for the Exp-01 ~ Exp-02 and Exp-07 ~ Exp-08 groups are analysed. Figure 10 shows that Exp-01 (and Exp-02) outperforms Exp-07 (and Exp-08), indicating that including the cloud and non-cloud variables in the ensemble cycling makes the forecasting more skilful than cycling the cloud variables alone. The benefit **was** introduced to the non-cloud variables during the model integration.



470 **Figure 10.** The time evolution of (a) FSS and (b) MAE of the ensemble mean of the first-guess forecast and analysis of CWP for the cycled **DA** experiments designed to illustrate the sensitivity to cycling variables.

To demonstrate the error growth for the non-cloud variables, the temporal evolution of the ratio of benefits \beth , calculated by formula (15), is presented by Figure 11.

$$\beth = N_{bet}/N_{eff} \quad (15)$$

475 where N_{bet} denotes the number of horizontal grid boxes with negative differences of MPE between the analysis and the first guess (refer to Section 2.4 and Scheck et al., 2020), and N_{eff} denotes the number of observations effectively assimilated by the **DA** system (see the next section).

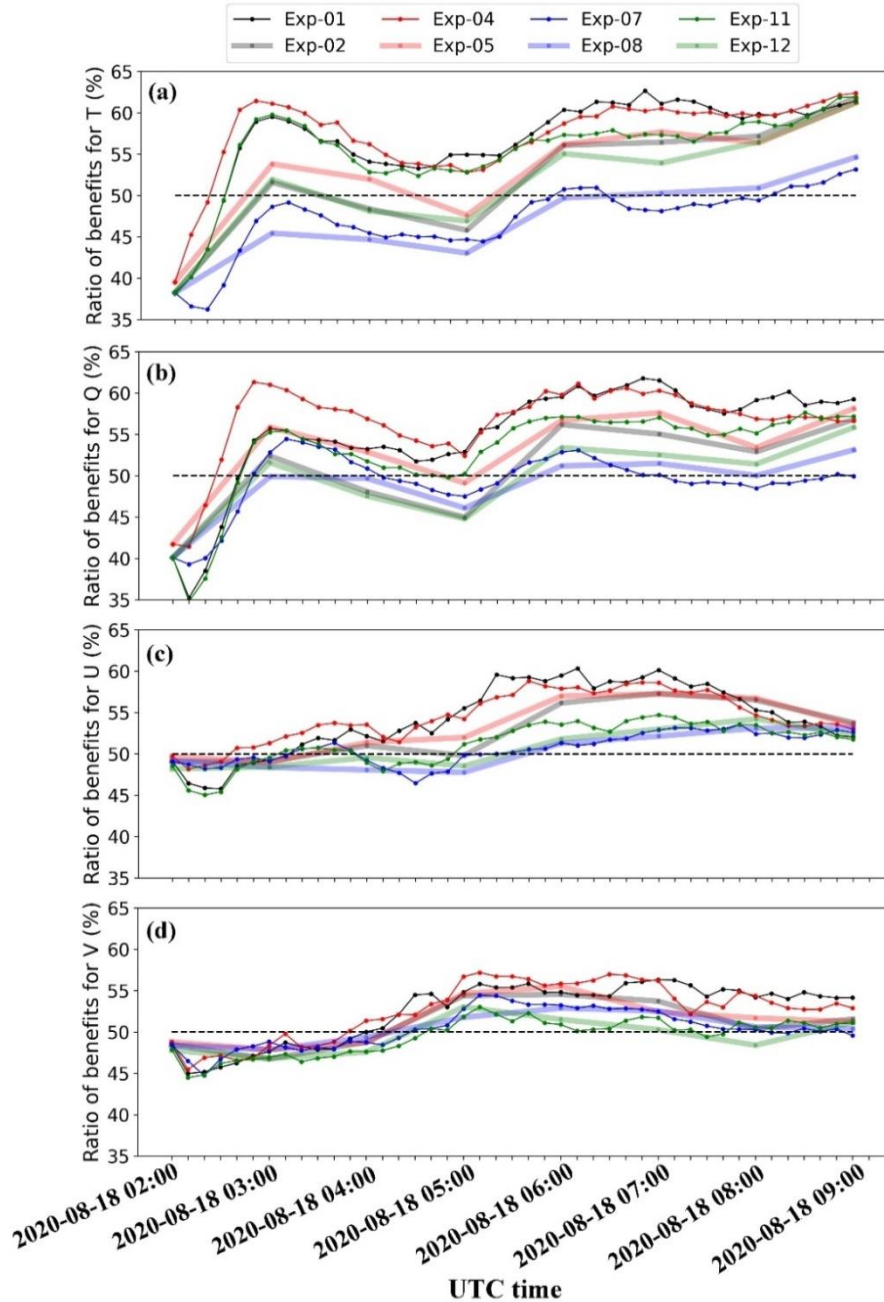


Figure 11. The time evolution of the ratio of beneficial **impact** Δ , calculated by Formula (15) for the first-guess forecast and analysis of (a) the **perturbation** potential temperature; (b) the water vapour mixing ratio; (c) the x-wind component; and (d) the y-wind component.

Figure 11 indicates positive **impact** of SW radiance **DA** on the major non-cloud variables, especially at the later cycling steps. We think that a main reason is the positive feedback to the non-cloud variables due to the adjustment to cloud variables during the WRF ensemble integration.

485 A potential explanation to the slightly positive **impact** of the **DA** on water vapour mixing ratio is given here. If the ensemble mean of the first-guess equivalent radiance is overestimated **for a cloud containing liquid hydrometeors**, Q_c tend to be decreased in the analysis field in order to match a negative analysis increment in the observation space. In the next ensemble forecast cycle, the grid boxes with decreased Q_c may generate more hydrometeors due to condensation. **This is because the supersaturation of surrounding atmosphere is increased due to a loss of some cloud hydrometeors (i.e., a loss of condensation surface). The increased supersaturation could activate new condensation nuclei and enhance the condensation process, which consumes more water vapour.** As a result, the VIS radiance could be positively related to the water vapour mixing ratio, and vice versa. According to Formula (4), the covariance between the VIS radiance and water vapour mixing ratio will adjust Q correctly.

490 The adjustment of temperature is more likely related to the interactions between clouds and radiation. For example, decreased CWP or CFC tends to enhance the direct radiation flux in the surface layer, increasing the low-level temperature toward the truth as indicated by Scheck et al. (2020), and vice versa. In addition, the interactions between clouds and longwave radiation tend to generate cooling effects at cloud top and heating effects at cloud bottom (Zhang et al., 2020). Therefore, a relationship between cloud radiance and temperature is expected, and the covariance between VIS radiance and temperature could adjust T correctly.

495 500 The **impact** of SW radiance **DA** on the x- and y-wind components **is** slightly negative before 04:00 UTC, and becomes positive thereafter. We think that the positive **impact is** mainly caused by the convergence and divergence related to the thermal instability, which is closely related to cloud formation (increased radiance) and dissipation (decreased radiance) for the convective systems. As the cloud-radiation interactions modify the temperature profile, the change of clouds could strengthen or weaken the thermal instability and **impact** the z-wind component. The z-wind component is closely related to 505 horizontal x- and y-wind components by adjusting the convergence and divergence (White et al., 2018). Therefore, an indirect “radiance-cloud-vertical velocity-convergence and divergence-horizontal wind” interaction could map the observation increment to the U and V increments.

c. Influences of outlier threshold values

510 Not all observations were effectively assimilated by the WRF/DART-RTTOV system. Some of the observations were rejected by the **DA** system due to two reasons: 1) existence of non-monotonic pressures, i.e., pressure increases with altitude. This situation was generated at some points by the improper interpolation of the perturbed first-guess model state to the RTTOV pre-defined layers. For this case study, non-monotonic pressures were mainly located in the Qinghai-Tibet Plateau, Tianshan Mountain, and Central Taiwan ranges (not shown for simplicity), where complex high terrain exists; 2) the differences between the observations and the first-guess ensemble mean equivalent observations are too large and 515 assimilating these data may cause collapse of WRF model. For the observations rejected due to the second reason, the ratio of observations to be assimilated is mainly determined by setting an outlier threshold value. Increasing the outlier threshold value could increase **the ratio of observations effectively assimilated** (Figure 12), but it may introduce unstable adjustments to model state variables and destroy the forecast. Therefore, **a trade-off between large outlier threshold value and the**

potentially detrimental effects on forecasts should be assessed. The analysis and 10 min, 1 hr, and 3 hr first-guess forecasts indicate improved results when increasing the outlier threshold values (Figure 13) and an outlier threshold value of 6 does not cause the collapse of WRF and generates improvements to the analysis and first-guess forecasts of CWP and cloud coverage.

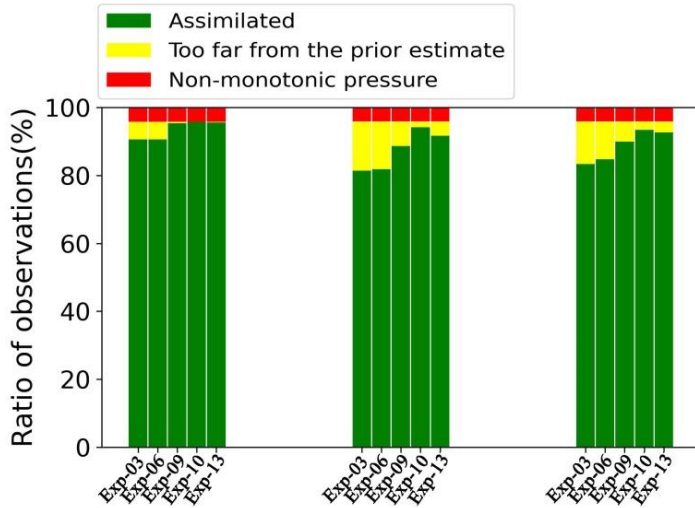


Figure 12. The ratio of observations assimilated or rejected by the WRF-DART system for different experiment designs with different outlier threshold values and observation errors.

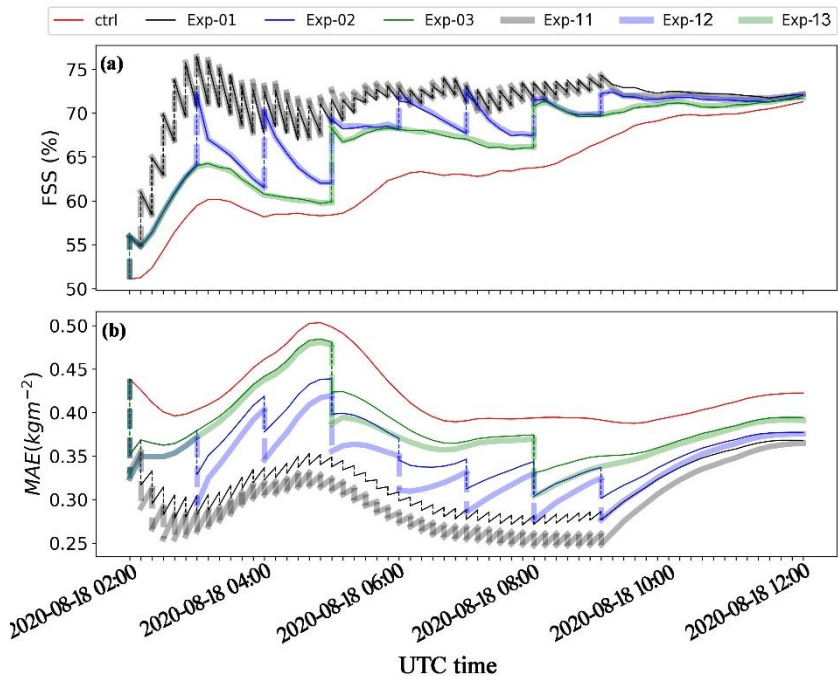
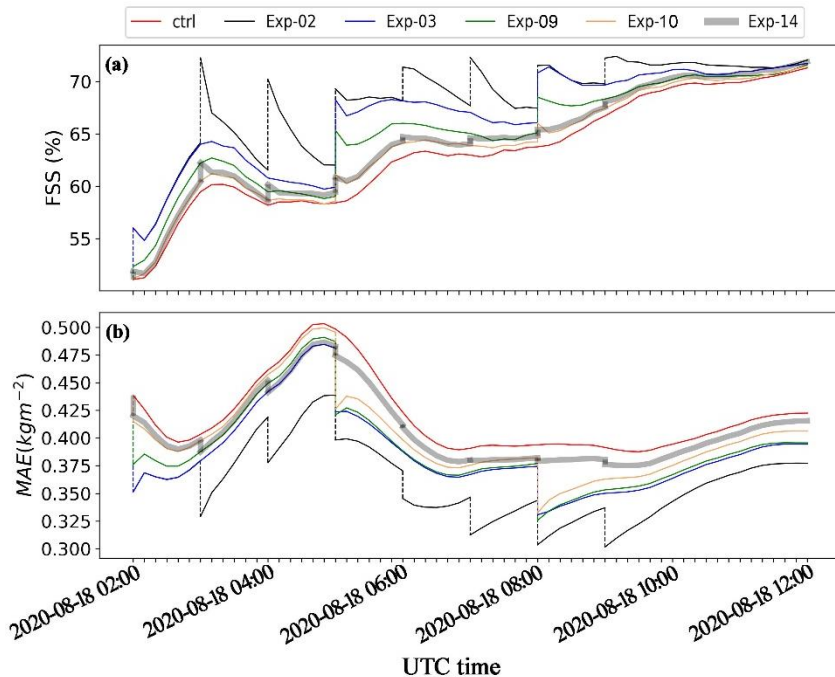


Figure 13. The time evolution of (a) FSS and (b) MAE of the ensemble mean of the first-guess forecast and analysis of CWP for cycled DA experiments with different outlier threshold values.

530 **d. Influences of observation errors and thinning**

530 The ratio of observations effectively assimilated is also influenced by the observation errors. Enlarging the observation errors will retain larger ratio of observations effectively assimilated (Figure 12). However, increasing observation errors implies less weight assigned to the observations during the DA. Therefore, the analysis and first-guess forecast are influenced by the observation errors in both ways with a trade-off. To evaluate the influences, FSS and MAE of the ensemble mean CWP for the cycled DA experiments with different observation errors are presented in Figure 14. The 535 analysis and first-guess forecasts of CWP and cloud coverage are negatively related to the observation errors. As a complementary to the parameters controlling the number of observations, the influences by thinned observations (Exp-14) were presented. The results indicate that thinning observation only resulted in slight improvements.



540 **Figure 14. The time evolution of (a) FSS and (b) MAE of the ensemble mean of the first-guess forecast and analysis of CWP for the cycled DA experiments with varying observation errors and observation pre-processing (with and without thinning).**

3.2.2 Impact on precipitation

The first-guess forecast of rain rate for the nature run, control run, Exp-01, and Exp-11 are shown in Figure 15. On the domain average, the rain rates were overestimated by both control and cycled DA experiments. Compared with the control run, the precipitation for the cycled DA experiments was decreased in most cases, and the spatial distribution of the 545 precipitation agreed better with the nature run (Figure 16(a)).

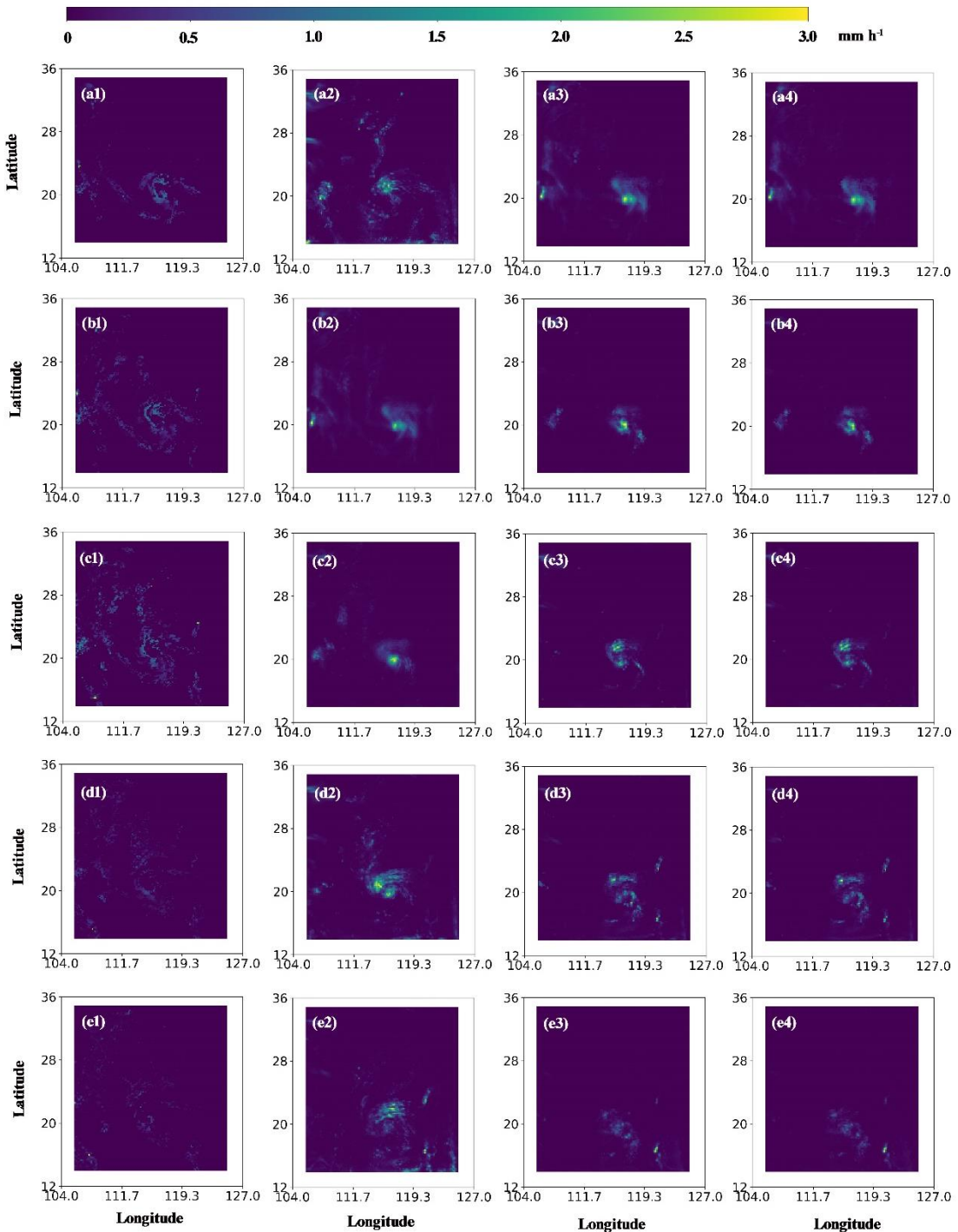


Figure 15. The time evolution of the rain rate for the nature run (column 1), control run (column 2), first-guess forecast of Exp-01 (column 3) and Exp-11(column 4). From top to bottom, the row panels correspond to the results for 02:00~02:10, 04:00~04:10, 06:00~06:10, 08:00~08:10, and 10:00~10:10 UTC 18 August 2020.

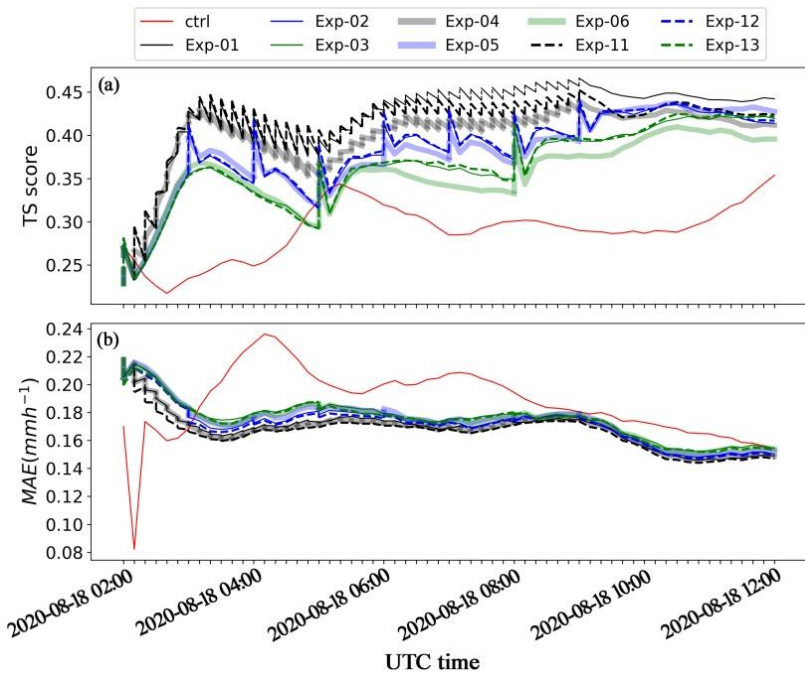


Figure 16. The time evolution of (a) the TS score and (b) MAE of the ensemble mean of the first-guess forecast of rain rate.

The metrics of the rain rate forecast indicate that the forecasting skills were improved at most analysis times (Figure 16(b)). However, the improvements on rain rate did not happen at all times. For example, at the initial cycling step (before 555 04:00 UTC, August 18, 2020), the control run seemed to outperform the cycled DA experiments. As the time progressed, the advantages of assimilating VIS radiance data became apparent. The improved TS score was closely related to the improved CWP and cloud coverage. It is noted that the improvements on the rain rate were not as significant as CWP. Some studies indicated that precipitation was closely related to cloud vertical structure (Kubar and Hartmann, 2008; Yan et al., 2019), the presence and distribution of liquid and ice hydrometeors (Field and Heymsfield, 2015; Mühlstädt et al., 2015; Korolev et 560 al., 2017), surrounding atmosphere and dynamic state variables (Kanji et al., 2017), etc. Therefore, the impact of the SW radiance DA on the rain rate suffers from its inability to constrain cloud vertical structures, improve cloud phase simulations, and correct cloud location errors (underestimation), etc., as discussed in the previous sections.

4. Conclusions and future works

In this study, a series of single observation experiments and cycled DA experiments were performed in an OSSE framework 565 to evaluate the WRF/DART-RTTOV system for assimilating FY-4A/AGRI VIS (channel 2) radiance data. The single observation experiments were designed to reveal the positive impact and limitations of assimilating satellite VIS radiance data on the cloud variables (liquid/ice water mixing ratio and CWP, effective radius of liquid water droplets, and cloud

fraction) and non-cloud variables (water vapour mixing ratio, perturbation potential temperature, and wind). The cycled DA experiments were designed to explore the **impact** of assimilating VIS radiance data on the analysis and first-guess forecasts of a tropical storm case with different model settings and observation pre-processing, including varying the filter algorithms, cycling variables, updating frequencies, outlier thresholds, observation errors, and **observation thinning**. The main findings are as follows.

(1) Single observation experiments exhibit that assimilating the satellite VIS radiance data generated overall positive impact on cloud variable analysis for the first DA cycle although in some rare cases, the DA increased the errors both in the observation space and in the cloud variable (or diagnosed parameter CWP) space. The negative **impact** was closely related to the non-linear properties of the forward operator and the non-Gaussian properties of the first-guess probability distribution function. In addition, neutral **impact** was revealed on non-cloud variables including water vapour mixing ratio, temperature, and horizontal winds.

(2) Although neutral **impact** was revealed for the non-cloud variables in the first DA cycle, both non-cloud variables and cloud variables were improved in the following-on ensemble forecast and DA cycles. The beneficial impact on the non-cloud variables was closely related to the analysis increments of cloud variables by condensation/evaporation and deposition/sublimation processes, and cloud-radiation interactions of the model microphysics. The RHF filter slightly outperformed the EAKF filter due to its ability to deal with the non-Gaussian problems, nevertheless at a cost of ~1.8 times of more computational time.

(3) The cycled DA experiments revealed that the first-guess forecast and analysis are positively related to increasing the outlier threshold value and the updating frequency, and negatively related to increasing observation errors and thinning length scale. Similar results were found for the precipitation forecasts. Assimilating the SW radiance data effectively improved the representation of locations with or without precipitation, but less for the quantitative metrics of the rain rate. The limited **impact** on the rain rate is due to the fact that the DA scheme is not effective to constrain cloud vertical structures, modifying cloud phases, and correcting cloud location errors in the case of underprediction that caused zero-spread problem.

The findings in this study provide useful guidance on setting WRF/DART-RTTOV configurations and pre-processing of observations for assimilating the FY-4A and the upcoming FY-4B VIS radiance data in real-time models. This study complements to Scheck et al. (2020) who reported the potentials and limitations of assimilating the Meteosat SEVERI VIS imagery with the COSMO/KENDA system using LETKF. In general, the pros and cons of assimilating the VIS radiance data found in this study agrees to those in Scheck et al. (2020), except that slightly positive **impact** on horizontal wind speeds was found in this study while Scheck et al. (2020) reported neutral **impact**. We tentatively ascribe the positive **impact** on U and V to the convergence or divergence related to the “radiance—cloud—vertical velocity—convergence and divergence—horizontal winds” interaction and it should differ in weather systems. Therefore, the different **impact** on horizontal winds of the two studies could be caused by the differences in the weather systems studied. In addition, the two studies used different the models/tools and corresponding configurations and this study explored the properties unique to the WRF/DART system.

It is noteworthy that the present study was based on the low-resolution model simulations at $15\text{ km} \times 15\text{ km}$. Such grid spacing is large enough to avoid radiance simulation errors due to 3D radiative effects, which are apparent for high-resolution simulations (V  nai and Marshak, 2001). Although the 3D radiative transfer effects could be properly corrected by some of the forward operators in RTTOV, the related parameters and datasets specific to FY-4A/AGRI are currently unavailable. Further studies should be extended to cloud-resolving model simulations like Scheck et al. (2020) to fully take the advantage of high-resolution satellite VIS radiance data. **Meanwhile**, some attention should be paid to the forward operator because the enhanced 3D radiative effects in high-resolution modelling **may** cause the nonlinearity of forward operator more complicated. An outlook of future works is summarized below.

(1) **To tune up the forward operators and more accurately estimate the observation errors.** The findings in this study suggest that decreasing observation errors improves the first-guess forecast and analysis. One of the factors determining the observation errors is the forward operator (Janji   et al., 2017). Therefore, it is necessary to tune up the RTTOV configurations in simulating synthetic FY-4A visible imagery from WRF model state variables and to estimate the observation errors under different modelling resolutions, weather conditions, sun-viewing geometries, etc. Scheck et al. (2018) assessed the performance of the forward operator MFASIS by comparing the synthetic visible imagery simulated based on the state variables from COSMO with the SEVIRI visible image. These works could be referenced when assessing the performance of RTTOV simulations against FY-4A visible observations.

(2) **To improve the computational efficiency and accuracy of the forward operators.** Assimilating visible radiance data is quite time-consuming for the current WRF/DART-RTTOV system (around 7 min in an EAKF cycle and 13 min in a RHF cycle). Increasing the updating frequency and outlier threshold value makes the computational cost even more expensive. We need an accurate and fast observation operator for assimilating the FY-4A (and the upcoming FY-4B) visible radiance data at both low- and high-resolution simulations. Scheck et al. (2016a, 2021) developed a Look-up Table (LUT) and machine learning based forward operator that is several orders faster than DOM-based methods. In addition, three-dimensional radiative effects could be corrected for high-resolution modelling without adding too expensive computation cost (Scheck et al., 2018; Albers et al., 2020; Zhou et al., 2021). These methods should be explored to improve forward operators suitable for assimilating the FY-4A visible radiance data.

(3) **To correct the errors due to the non-Gaussian and non-linear problems with the SW radiance DA.** The performance of EAKF was limited in dealing with the non-linear and non-Gaussian problems. The Particle Filter (PF) is declared to have advantages in dealing with the non-Gaussian and non-linear problems. With certain localized method included, PF shows great potential in application to high-dimension numerical prediction model such as the WRF model (Shen and Tang, 2015; Poterjoy, 2016; Pinheiro et al., 2019). Therefore, some newly-developed PF methods could be a candidate to further improve the forecasting skills of WRF model with the **DA** of satellite visible radiance.

(4) **To develop techniques to reduce the cloud location errors.** The performance of WRF/DART system is limited to correct the cloud location errors in the case that the first guess underpredicts clouds or a zero spread of prior ensemble members occurs. Dowell et al. (2012) proposed a method to tackle the location errors in assimilating radar data by EnKF.

Their basic idea was to add some perturbations to the base state randomly and add local perturbations in and near precipitation areas regularly to produce clouds in the precipitation areas. In addition, White et al. (2018) also promoted a method to produce clouds comparable to satellite observations, but this method needs additional observations (such as brightness temperature at infrared bands) to support. Improvement on horizontal cloud location errors could improve precipitation forecasts in some cases. For example, the vertical cloud structure is less important for some deep convection since the cloud may extend from boundary layer up to troposphere (Hu et al., 2021).

(5) To evaluate the impact of assimilating FY-4A visible radiance data for long-term forecasts. The limited impact of the DA on rain rate is partly caused by the shortcomings of the DA procedure discussed above, but by the spin-up effects as well. The spin-up effects may introduce false alarm precipitation due to the interactions between the model dynamics and microphysics when smaller scales are now well represented in the initial conditions and lateral boundary conditions (Short and Petch, 2022). In this study, we started to assimilate the synthetic FY-4A visible radiance data after 2-hour cold start and run the model for 10-hour forecast (02:00 ~ 12:00 UTC). This is a too short time period to exclude the spin up. Improvements on precipitation should be expected for longer forecasts.

Finally, for the real FY-4A visible radiance DA, the NWP model errors on cloud and precipitation forecasts should be considered in the DA processes. On one hand, the parameterization (such as the subgrid-scale cloud fraction parameterization in this study) is closely related to the calculation of synthetic visible radiance by a forward operator. On the other hand, the formation and dissipation of cloud and precipitation highly depend on the model parameterization. Suboptimal parameterization may introduce large model bias in some cases due to unsolved scales and processes (Janjić et al., 2021). The model bias could introduce negative impact on cloud and precipitation forecasts. Therefore, the NWP model should be tuned to properly represent the scale-dependent microphysical processes in order to fully realize the effects of the FY-4A visible radiance DA.

Code and data availability

Version 4.1.1 of WRF-ARW source code is publicly available at <http://www2.mmm.ucar.edu/wrf/users/>. The Manhattan release of DART source code (version 9.8.0), including the RTTOV observation operator (version 12.3), is publicly available at <https://dart.ucar.edu/>. Version 12.3 of RTTOV source code is publicly available at <https://nwp-saf.eumetsat.int/site/software/rttov/>. The NCEP FNL (Final) Operational Global Analysis data are downloaded from <https://rda.ucar.edu/datasets/ds083.2/>. The ERA5 hourly data are available at <https://cds.climate.copernicus.eu/api/v2/resources>. The source codes of WRF-ARW, WPS, RTTOV, and DART models (tool), as well as the input and (processed) output data, and the visualization scripts are available at <https://doi.org/10.5281/zenodo.7028828>.

Author contribution

Yongbo Zhou: Conceptualization, Methodology, Writing original draft, Visualization, Funding acquisition. Yubao Liu: Conceptualization, review and editing. Zhaoyang Huo, review and editing. Yang Li, review and editing.

Competing interests

670 The authors declare that they have no conflict of interest.

Acknowledgement

This study is supported by the Natural Science Foundation of Jiangsu Province (Grant No. BK0210665) and Startup Foundation for Introducing Talent of Nanjing University of Information Science and Technology (Grant No. 2019r095). **The work is also partly supported by the National Key R&D Program of China (Grant No. 2018YFC1507901).** We are grateful to

675 Glen Romine, Moha Gharamti, Nancy Collins, and Tim Hoar from the DART team at the National Center for Atmospheric Research (**NCAR**) for kindly providing instructions on running this tool. We acknowledge the High Performance Computing Center of Nanjing University of Information Science & Technology for their support of this work. We are grateful to the two anonymous reviewers for their constructive comments and suggestions.

References

680 Albers, S., Saleeby, M. S., Kreidenweis, S., Bian, Q., Xian, P., Toth, Z., Ahmadov, R., James, E., and Miller, D. S.: A fast visible-wavelength 3D radiative transfer model for numerical weather prediction visualization and forward modeling, *Atmos. Meas. Tech.*, 13, 3235–3261, doi: 10.5194/amt-13-3235-2020, 2020.

Anderson, J. L.: An Ensemble Adjustment Kalman Filter for Data Assimilation, *Mon. Weather Rev.*, 129, 2884-2903, doi:10.1175/1520-0493(2001)129<2884:AEAKFF>2.0.CO;2, 2001.

685 Anderson, J. L.: An adaptive covariance inflation error correction algorithm for ensemble filters, *Tellus A*, 59, 210-224, doi:10.1111/j.1600-0870.2006.00216.x, 2007.

Anderson, J. L.: Spatially and temporally varying adaptive covariance inflation for ensemble filters, *Tellus A*, 61, 72–83, doi:10.1111/j.1600-0870.2008.00361.x, 2009.

Anderson, J. L.: Localization and Sampling Error Correction in Ensemble Kalman Filter Data Assimilation, *Mon. Wea. Rev.*, 690 140(7), 2359-2371, doi:10.1175/MWR-D-11-00013.1, 2012.

Anderson, J. L.: A Non-Gaussian Ensemble Filter Update for Data Assimilation, *Mon. Wea. Rev.*, 138(11): 4186–4198, doi: 10.1175/2010MWR3253.1, 2010.

Anderson, J., Hoar, T., Raeder, K., Liu, H., Collins, N., Torn, R., and Avellano, A.: The Data Assimilation Research Testbed: A Community Facility, *B. Am. Meteorol. Soc.*, 90(9), 1283-1296, doi:10.1175/2009BAMS2618.1, 2009.

695 Baren, A. J., Cotton, R., Furtado, K., Havemann, S., Labonne, L.-C., Marenco, F., Smith, A., and Thelen, J.-C.: A self-consistent scatteringmodel for cirrus. II: The high and low frequencies, *Q. J. R. Meteorol. Soc.*, 140: 1039-1057, doi:10.1002/qj.2193, 2014.

Bauer, P., Geer, J. A., Lopez, P., and Salmond, D.: Direct 4D-Var assimilation of all-sky radiances. Part I: Implementation, *Q. J. R. Meteorol. Soc.*, 136(152): 1868-1885, doi: 10.1002/qj.659, 2010.

700 Bauer, P., Ohring, G., Kummerow, C., and Auligne, T.: Assimilating satellite observations of clouds and precipitation into NWP models, *B. Am. Meteorol. Soc.*, 92, ES25-ES28, doi:10.1175/2011BAMS3182.1, 2011.

Bretherton, C. S., and Park, S.: A New Moist Turbulence Parameterization in the Community Atmosphere Model, *J. Clim.*, 22, 3422-3448, doi: 10.1175/2008JCLI2556.1, 2009.

Buehner, M., Houtekamer, P. L., Charette, C., Mitchell, H. L., and He, B.: Intercomparison of Variational Data Assimilation 705 and the Ensemble Kalman Filter for Global Deterministic NWP. Part I: Description and Single-Observation Experiments, *Mon. Wea. Rev.*, 138(5): 1550-1566, doi: 10.1175/2009MWR3157.1, 2013.

Carminati, F. , and Migliorini, S.: All-sky Data Assimilation of MWTS-2 and MWHS-2 in the Met Office Global NWP System, *Adv. Atmos. Sci.*, 38: 1682-1694, doi: 10.1007/s00376-021-1071-5, 2021.

Coste, P., Pasternak, F., Faure, F., Jacquet, B., Bianchi, S., Aminou, D. M. A., Luhmann, H. J., Hanson, C., Pili, P., and 710 Fowler, G.: SEVIRI, the imaging radiometer on Meteosat second generation: in-orbit results and first assessment, *Proceedings of the SPIE*, 10568, 105680L, doi:10.1117/12.2308023, 2017.

Di, Z., Gong, W., Gan, Y., Shen, C., and Duan, Q.: Combinatorial Optimization for WRF Physical Parameterization Schemes: A Case Study of Three-Day Typhoon Simulations over the Northwest Pacific Ocean, *Atmosphere*, 10(5), 233; doi: 10.3390/atmos10050233, 2019.

715 Dowell, D. C., Wicker, L. J., and Snyder, C.: Ensemble Kalman Filter Assimilation of Radar Observations of the 8 May 2003 Oklahoma City Supercell: Influences of Reflectivity Observations on Storm-Scale Analyses, *Mon. Wea. Rev.*, 139(1): 272-294, doi: 10.1175/2010MWR3438.1

Dudhia, J.: A Multi-layer Soil Temperature Model for MM5, *Preprints, Sixth PSU/NCAR Mesoscale Model Users' Workshop*, Boulder, 22-24 July 1996, pp. 49-50

720 Field, P. R., and Heymsfield, A. J.: Importance of snow to global precipitation, *Geophys. Res. Lett.*, 42, 9512-9520, doi: 10.1002/2015GL065497, 2015.

Gao, J. D., Xue, M., and Stensrud, D. J.: The Development of a Hybrid EnKF-3DVAR Algorithm for Storm-Scale Data Assimilation, *Adv. Meteorol.*, 2013, 512656, doi: 10.1155/2013/512656, 2013.

Geer, A. J., Bauer, P., and O'Dell, C. W.: A revised cloud overlap scheme for fast microwave radiative transfer in rain and 725 cloud, *J. Appl. Meteorol. Clim.*, 48, 2257–2270, doi: 10.1175/2009JAMC2170.1, 2009.

Geer, A. J., Lonitz, K., Weston, P., Kazumori, M., Okamoto, K., Zhu, Y., Liu, H. E., Collard, A., Bell, W., Migliorini, S., Chambon, P., Fourrié, N., Kim, M.-J., Köpken-Watts, C., and Schraff, C.: All-sky satellite data assimilation at operational weather forecasting centres, *Q. J. R. Meteorol. Soc.*, 144(713): 1191-1217, doi: 10.1002/qj.3202, 2017.

Geer, A. J., Migliorini, S., and Matricardi, M.: All-sky assimilation of infrared radiances sensitive to mid- and upper-
730 tropospheric moisture and cloud, *Atmos. Meas. Tech.*, 12, 4903-4929, doi:10.5194/amt-12-4903-2019, 2019.

Hasselmann, K., Barnett, T. P., Bouws, E., Carlson, H., Cartwright, D. E., Enke, K., Ewing, J. A., Gienapp, H., Hasselmann, D. E., Kruseman, P., Meerburg, A., Müller, P., Olbers, D. J., Richter, K., Sell, W., and Walden, H.: Measurements of wind-wave growth and swell during the Joint North Sea Wave Project (JONSWAP), *Deutches Hydrographisches Institut*, 12, 95 pp., <http://resolver.tudelft.nl/uuid:f204e188-13b9-49d8-a6dc-4fb7c20562fc>, 1973.

735 Hu, J., Fu, Y., Zhang, P., Min, Q., Gao, Z., Wu, S., and Li, R.: Satellite Retrieval of Microwave Land Surface Emissivity under Clear and Cloudy Skies in China Using Observations from AMSR-E and MODIS, *Remote Sens.*, 13(19), 3980, doi: 10.3390/rs13193980, 2021a.

Hu, X., Ge, J., Li, W., Du, J., Li, Q., and Mu, Q.: Vertical structure of tropical deep convective systems at different life stages from CloudSat observations, *J. Geophys. Res.*, 126, e2021JD035115, doi: 10.1029/2021JD035115, 2021b.

740 Iacono, M. J., Delamere, J. S., Mlawer, E. J., Shephard, M. W., Clough, S. A., and Collins, W. D.: Radiative forcing by long-lived greenhouse gases: Calculations with the AER radiative transfer models, *J. Geophys. Res.*, 113, D13103, doi:10.1029/2008JD00944, 2008.

Janjić, T., Bormann, N., Bocquet, M., Carton, J. A., Cohn, S. E., Dance, S. L., Losa, S. N., Nichols, N. K., Potthast, R., Waller, J. A., Weston P., On the representation error in data assimilation, *Q. J. R. Meteorol. Soc.*, 144(713): 1257-1278, doi: 10.1002/qj.3130, 2017

745 Jiménez, A., P., Dudhia, J., González-Rouco, J. F., Navarro, J., Montávez, P. J., and García-Bustamante, E.: A Revised Scheme for the WRF Surface Layer Formulation, *Mon. Wea. Rev.*, 140(3): 898–918, doi: 10.1175/MWR-D-11-00056.1, 2012.

Kanji, A. J., Ladino, L. A., Wex, H., Boose, Y., Burkert-Hohn, M., Cziczo, D. J., and Krämer, M.: Overview of Ice
750 Nucleating Particles, *Meteor. Monographs*, 58(1), 1.1–1.33, doi: 10.1175/AMSMONOGRAPHS-D-16-0006.1, 2017

Keat, W. J., Stein, T. H. M., Phaduli, E., Landman, S., Becker, E., Bopape, M.-J. M., Hanley, K. E., Lean, H. W., and Webster, S.: Convective initiation and stormlife cycles in convection-permitting simulations of the Met Office Unified Model over South Africa, *Q. J. R. Meteorol. Soc.*, 145, 1323-1336, doi:10.1002/qj.3487, 2019.

Kostka, P. M., Weissmann, M., Buras, R., Mayer, B., and Stiller, O.: Observation operator for visible and near-infrared
755 satellite reflectances, *J. Atmos. Ocean. Tech.*, 31(6), 1216-1233, doi:10.1175/JTECH-D-13-00116.1, 2014.

Kubar, L. T., and Hartmann, D. L.: Vertical structure of tropical oceanic convective clouds and its relation to precipitation, *Geophys. Res. Lett.*, 35, L03804, doi: 1029/2007GL032811, 2008.

Korolev, A., McFarquhar, G., Field, P. R., Franklin, C., Lawson, P., Wang, Z., Williams, E., Abel, S. J., Axisa, D., Borrman, S., Crosier, J., Fugal, J., Krämer, M., Lohmann, U., Schlenczek, O., Schnaiter, M., and Wendisch, M.:

760 Mixed-Phase Clouds: Progress and Challenges, Meteor. Monographs, 58(1), 5.1–5.50, doi: 10.1175/AMSMONOGRAPHSD-17-0001.1, 2017.

Kurzrock, F., Nguyen, H., Sauer, J., Ming, F. C., Cros, S., Smith Jr. W. L., Minnis, P., Palikonda, R., Jones, T. A., Lallemand, C., Linguet, L., and Lajoie, G.: Evaluation of WRF-DART (ARW v3.9.1.1 and DART Manhattan release) multiphase cloud water path assimilation for short-term solar irradiance forecasting in a tropical environment, *Geosci. Model Dev.*, 12, 3939–3954, doi:10.5194/gmd-12-3939-2019, 2019.

765 Lawson, W. G., and Hansen, J. A.: Implications of Stochastic and Deterministic Filters as Ensemble-Based Data Assimilation Methods in Varying Regimes of Error Growth, *Mon. Wea. Rev.*, 132 (8), 1966–1981, doi: 10.1175/1520-0493(2004)132<1966:IOSADF>2.0.CO;2, 2004.

Lei, J., Bikel, P., and Snyder, C.: Comparison of Ensemble Kalman Filters under Non-Gaussianity, *Mon. Wea. Rev.*, 138 (4): 770 1293–1306, doi: 10.1175/2009MWR3133.1, 2010.

Lei, L., Anderson, J. L., and Romine, G. S.: Empirical Localization Functions for Ensemble Kalman Filter Data Assimilation in Regions with and without Precipitation, *Mon. Wea. Rev.*, 143(9), 3664–3679, doi:10.1175/MWR-D-14-00415.1, 2015.

Li, J., Geer, J. A., Okamoto, K., Otkin. A. J., Liu, Z., Han, W., and Wang, P.: Satellite All-sky Infrared Radiance Assimilation: Recent Progress and Future Perspectives, *Adv. Atmos. Sci.*, 39(1): 9–21, doi: 10.1007/s00376-021-1088-9, 775 2022.

Ma, Z., Maddy, E. S., Zhang, B., Zhu, T., Boukabara, S. A.: Impact Assessment of Himawari-8 AHI Data Assimilation in NCEP GDAS/GFS with GSI, *J. Atmos. Ocean. Tech.*, 34(4), 797–815, doi:10.1175/JTECH-D-16-0136.1, 2017.

Matricardi, M.: The generation of RTTOV regression coefficients for IASI and AIRS using a new profile training set and a 780 new line-by-line database, ECMWF, Technical Memorandum, 564, 47 pp., <https://doi.org/10.21957/59u3oc9es>, 2008.

Mayer, B., and Kylling, A.: Technical note: The libRadtran software package for radiative transfer calculations—description and examples of use, *Atmos. Chem. Phys.*, 5, 1855–1877, doi:10.5194/acp-5-1855-2005, 2005.

McCarty, W., Jedlovec, G., and Timothy L. M.: Impact of the assimilation of Atmospheric Infrared Sounder radiance 785 measurements on short-term weather forecasts, *J. Geophys. Res.*, 144, D18122, doi: 10.1029/2008JD011626, 2009.

Migliorini, S. and Candy, B.: All-sky satellite data assimilation of microwave temperature sounding channels at the Met Office, *Q. J. R. Meteorol. Soc.*, 145(719), 867–883, doi:10.1002/qj.3470, 2019.

Mittermaier, M., Roberts, N., Thompson, S. A.: **A long-term assessment of precipitation forecast skill using the Fractions Skill Score, *Meteorol. Appl.*, 20: 176 – 186, doi: 10.1002/met.296, 2013.**

Müllmenstdt, J., Sourdeval, O., Delano   J., and Quaas, J.: Frequency of occurrence of rain from liquid-, mixed-, and ice- 790 phase clouds derived from A-Train satellite retrievals, *Geophys. Res. Lett.*, 42, 6502–6509, doi: 10.1002/2015GL064604, 2015.

Nakajima T., and King, M. D.: Determination of the optical thickness and effective particle radius of clouds from reflected solar radiation measurements. Part I: Theory, *J. Atmos. Sci.*, 47(15): 1878-1893, doi:10.1175/1520-0469(1990)047<1878:DOTOTA>2.0.CO;2, 1990.

795 Pinheiro, F. R., van Leeuwen, P. J., and Geppert, G.: Efficient nonlinear data assimilation using synchronization in a particle filter, *Q. J. R. Meteorol. Soc.*, 145:2510-2523, doi:10.1002/qj.3576.

Polkinghorne, R. and Vukicevic, T.: Data assimilation of cloud-affected radiances in a cloud-resolving model, *Mon. Wea. Rev.*, 139(3), 755-773. doi:10.1175/2010MWR3360.1, 2011.

Poterjoy, J.: A Localized Particle Filter for High-Dimensional Nonlinear Systems, *Mon. Wea. Rev.*, 144 (1), 59-76, doi:10.1175/MWR-D-15-0163.1, 2016.

800 Prates, C., Migliorini, S., English, S., and Pavelinc, E.: Assimilation of satellite infrared sounding measurements in the presence of heterogeneous cloud fields, *Q. J. R. Meteorol. Soc.*, 140: 2062-2077, doi: 10.1002/qj.2279, 2014.

Saunders, R., Hocking, J., Turner, E., Rayer, P., Rundle, D., Brunel, P., Vidot, J., Roquet, P., Matricardi, M., Geer, A., Bormann, N., and Lupu, C.: An update on the RTTOV fast radiative transfer model (currently at version 12). *Geosci. Model Dev.*, 11(7), 2717-2737, doi:10.5194/gmd-11-2717-2018, 2018.

805 Scheck, L.: A neural network based forward operator for visible satellite images and its adjoint, *J. Quant. Spectrosc. Radiat. Transf.*, 274, 107841, doi:10.1016/j.jqsrt.2021.107841, 2021.

Scheck, L., Frèrebeau, P., Buras-Schnell, R., and Mayer, B.: A fast radiative transfer method for the simulation of visible satellite imagery, *J. Quant. Spectrosc. Radiat. Transf.*, 175, 54-67. doi:10.1016/j.jqsrt.2016.02.008, 2016a.

810 Scheck, L., Hocking, J., and Saunders, R.: A comparison of MFASIS and RTTOV-DOM. Report of Visiting Scientist mission NWP_VS16_01 (Document ID, NWPSAF-MO-VS-054), EUMETSAT. Retrieved from https://nwpsaf.eu/vs_reports/nwpsaf-mo-vs-054.pdf, 2016b.

Scheck, L., Weissmann, M., and Bernhard, M.: Efficient Methods to Account for Cloud-Top Inclination and Cloud Overlap in Synthetic Visible Satellite Images, *J. Atmos. Ocean. Tech.*, 35, 665-685, doi:10.1175/JTECH-D-17-0057.1, 2018.

815 Scheck, L., Weissmann, M., and Bach, L.: Assimilating visible satellite images for convective-scale numerical weather prediction: A case-study, *Q. J. R. Meteorol. Soc.*, 146(732), 3165-3186, doi:10.1002/qj.3840, 2020.

Schmit, T. J., Lindstrom, S. S., Gerth, J. J., and Gunshor, M. M.: Applications of the 16 spectral bands on the Advanced Baseline Imager (ABI), *J. Operational Meteor.*, 6 (4), 33-46, doi:10.15191/nwajom.2018.0604, 2018.

Schrötle, J., Weissmann, M., Scheck, L., and Hutt, A.: Assimilating Visible and Infrared Radiances in Idealized Simulations of Deep Convection, *Mon. Wea. Rev.*, 148(11), 4357-4375, doi:10.1175/MWR-D-20-0002.1, 2020.

820 Shen, F., Xu, D., Min, J., Chu, Z., and Li, X.: Assimilation of radar radial velocity data with the WRF hybrid 4DEnVar system for the prediction of hurricane Ike (2008), *Atmos. Res.*, 234, 104771, doi: 10.1016/j.atmosres.2019.104771, 2020.

Shen, Z., and Tang, Y.: A modified ensemble Kalman particle filter for non-Gaussian systems with nonlinear measurement functions, *J. Adv. Model. Earth Syst.*, 7, 50–66, doi:10.1002/2014MS000373, 2015.

Short, C. J., and Petch, J.: Reducing the spin-up of a regional NWP system without data assimilation, *Q. J. R. Meteorol. Soc.*, 148(745): 1623-1643, doi: 10.1002/qj.4268, 2022.

Skamarock, W. C., Klemp, J. B., Dudhia, J., Gill, D. O., Barker, D. M., Duda, M. G., Wang, X.-Y., Wang, W., and Power, J. G.: A Description of the Advanced Research WRF Version 3 (No. NCAR/TN-475+STR), University Corporation for Atmospheric Research, doi:10.5065/D68S4MVH, 2008.

830 Stengel, M., Lindskog, M., Undén, P., and Gustafsson, N.: The impact of cloud-affected IR radiances on forecast accuracy of a limited-area NWP model, *Q. J. R. Meteorol. Soc.*, 139(677): 2081-2096, doi: 10.1002/qj.2102, 2013.

Thompson, G., P. R. Field, R. M. Rasmussen, and W. D. Hall, 2008: Explicit forecasts of winter precipitation using an improved bulk microphysics scheme. Part II: implementation of a new snow parameterization, *Mon. Wea. Rev.*, 136: 5095-5115, doi: 10.1175/1520-0493(2004)132<5095:EFOWPU>2.0.CO;2, 2008

835 Tiedtke, M.: A comprehensive mass flux scheme for cumulus parameterization in large-scale models, *Mon. Wea. Rev.*, 117: 1779–1800, doi: 10.1175/1520-0493(1989)117<1779:ACMFSF>2.0.CO;2, 1989.

Vidot, J., and Borbás, É.: Land surface VIS/NIR BRDF atlas for RTTOV-11: model and validation against SEVIRI land SAF albedo product, *Q. J. R. Meteorol. Soc.*, 140, 2186-2196, doi:10.1002/qj.2288, 2014.

840 Vidot, J., Brunel, P., Dumont, M., Carmagnola, C., and Hocking J.: The VIS/NIR Land and Snow BRDF Atlas for RTTOV: Comparison between MODIS MCD43C1 C5 and C6, *Remote Sens.*, 10(1), 21, doi:10.3390/rs10010021, 2018.

Vukicevic, T., Greenwald, T., Zupanski, M., Zupanski, D., Vondar Harr, T., and Jones, A. S.: Mesoscale cloud state estimation from visible and infrared satellite radiance. *Mon. Wea. Rev.*, 132(12): 3066-3077. doi:10.1175/MWR2837.1, 2004.

845 Várnai T. and Marshak A.: Statistical Analysis of the Uncertainties in Cloud Optical Depth Retrievals Caused by Three-Dimensional Radiative Effects, *J. Atmos. Sci.*, 58(12), 1540-1548, doi:10.1175/1520-0469(2001)058<1540:SAOTUI>2.0.CO;2, 2001.

White, A. T., Pour-Biazar, A., Doty, K., Dornblaser, B., and McNider, R. T.: Improving Cloud Simulation for Air Quality Studies through Assimilation of Geostationary Satellite Observations in Retrospective Meteorological Modeling, *Mon. Wea. Rev.*, 146(1): 29-48, doi: 10.1175/MWR-D-17-0139.1, 2018.

Xu, D., Min, J., Shen, F., Ban, J., and Chen, P.: Assimilation of MWHS radiance data from the FY-3B satellite with the WRF Hybrid-3DVAR system for the forecasting of binary typhoons, *J. Adv. Model. Earth Syst.*, 8(2): 1014-1028, doi: 10.1002/2016MS000674, 2016.

850 Xu, K.-M., and Randall, A. D.: A Semiempirical Cloudiness Parameterization for Use in Climate Models, *J. Atmos. Sci.*, 53(21): 3084–3102, doi: 10.1175/1520-0469(1996)053<3084:ASCPFU>2.0.CO;2, 1996.

Xue, J. S.: Scientific issues and perspective of assimilation of meteorological satellite data, *Acta Meteorol. Sin.*, 67(9), 903-911, 2009, <https://doi.org/10.3321/j.issn:0577-6619.2009.06.001>, 2009 (in Chinese with English abstract).

Yan, Y., and Liu, Y.: Vertical Structures of Convective and Stratiform Clouds in Boreal Summer over the Tibetan Plateau and Its Neighboring Regions, *Adv. Atmos. Sci.*, 36 (10), 1089–1102, doi: 10.1007/s00376-019-8229-4, 2019.

860 Yang, C., Liu, Z., Bresch, J., Rizvi, S. R. H., Huang, X.-Y., and Min, J.: AMSR2 all-sky radiance assimilation and its impact on the analysis and forecast of Hurricane Sandy with a limited-area data assimilation system, *Tellus A: Dynamic Meteorology and Oceanography*, 68:1, 30917, doi: 10.3402/tellusa.v68.30917, 2016.

Yang, J., Zhang, Z., Wei, C., Lu, F., and Guo, Q.: Introducing the New Generation of Chinese Geostationary Weather Satellites, *Fengyun-4*, *B. Am. Meteorol. Soc.*, 98(8), 1737-1658, doi:10.1175/BAMS-D-16-0065.1, 2017.

865 Zhang, A. and Fu, Y.: Life Cycle Effects on the Vertical Structure of Precipitation in East China Measured by Himawari-8 and GPM DPR, *Mon. Wea. Rev.*, 146(7), 2183–2199, doi:10.1175/MWR-D-18-0085.1, 2018.

Zhang, C., Wang, Y. and Hamilton, K.: Improved Representation of Boundary Layer Clouds over the Southeast Pacific in ARW-WRF Using a Modified Tiedtke Cumulus Parameterization Scheme, *Mon. Wea. Rev.*, 139(11): 3489–3513, doi: 10.1175/MWR-D-10-05091.1, 2011.

870 Zhang, M., Zupanski, M., Kim, M.-J., and Knaff, J. A.: Assimilating AMSU-A Radiances in the TC Core Area with NOAA Operational HWRF (2011) and a Hybrid Data Assimilation System: Danielle (2010), *Mon. Wea. Rev.*, 141(11), 3889-2907, doi:10.1175/MWR-D-12-00340.1, 2013.

Zhang, P., Zhu, L., Tang, S., Gao, L., Chen, L., Zheng, W., Han, X., Chen, J., and Shao, J.: General Comparison of FY-4A/AGRI With Other GEO/LEO Instruments and Its Potential and Challenges in Non-meteorological Applications, *Front. Earth Sci.*, 6, 224, doi:10.3389/feart.2018.00224, 2019.

875 Zhang, T., Sun, J., and Yang, L.: A Numerical Study of Effects of Radiation on Deep Convective Warm Based Cumulus Cloud Development with a 3-D Radiative Transfer Model, *Atmosphere*, 11(11), 1187, doi: 10.3390/atmos11111187, 2020.

Zhou, Y. B., Liu, Y. B., Huo, Z. Y., and Li, Y.: WRF-DART/RTTOV input and (processed) output files for GMD-2022-30, 880 Zenodo, doi: [10.5281/zenodo.7028828](https://doi.org/10.5281/zenodo.7028828), 2022.

Zhou, Y. B., Liu, Y. B., and Liu, C.: A machine learning-based method to account for 3D Short-Wave radiative effects in 1D satellite observation operators, *J. Quant. Spectrosc. Radiat. Transf.*, 275, 107891, doi:10.1016/j.jqsrt.2021.107891, 2021.

Zhu, Y., Liu, E., Mahajan, R., Thomas, C., Groff, D., Van Delst, P., Collard, A., Treadon, R., and Derber, C. J.: All-Sky 885 Microwave Radiance Assimilation in NCEP's GSI Analysis System, *Mon. Wea. Rev.*, 144(12): 4709–4735, doi: 10.1175/MWR-D-15-0445.1, 2016.